Experimental Characterization of Front Propagation by Marangoni Forces in Ultrathin Liquid Films

Thesis by

Lisa Mannan Lee

In Partial Fulfillment of the Requirements

for the Degree of

Bachelor of Science in Physics

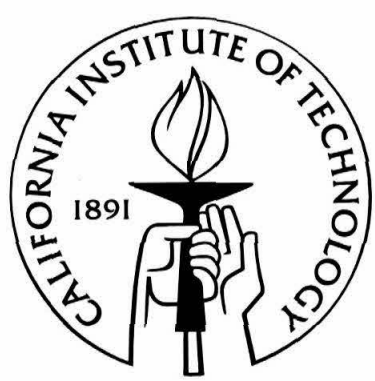

California Institute of Technology

Pasadena, California

2014

(Submitted May 9, 2014)

Acknowledgements

I would like to express my deepest appreciation to my mentor Sandra M. Troian for her support and guidance, not only on this project but also on my other paths of life. Her faith and enthusiasm in me, as well as her spontaneous bits of humor found in nearly any situation, have made this project an immense pleasure for me.

I would like to thank Kevin Fiedler for his help with lap equipment as well his endless invaluable advice. I would also like to thank Kelly Mauser with whom I collaborated on parts of this project, and Dr. Peter Thompson for his help with computer-related issues.

Lastly, I'd like to thank my parents for their support through all these years, and for teaching me the importance of persistence and loving what you do.

Abstract

Italian physicist Carlo Marangoni published a treatise in 1865 which first described the spontaneous flow of a liquid film caused by gradients in surface tension at a gas/liquid interface. Such gradients are established by variations in surface concentration of molecular species which lower the surface tension in proportion to the interface concentration. While the dynamics and power law behavior of the initial circular advancing front in surfactant coated films has been studied for about two decades, there has been relatively little work conducted on characterizing the fractal spreading patterns which develop behind this front. In this thesis, we examine the dynamics of front propagation and subsequent fractal evolution in ultrathin liquid films of glycerol driven to spread by concentration gradients in Aerosol OT, an insoluble anionic surfactant. We vary only the initial deposition volume and concentration while maintaining the initial liquid film thickness at 2.5 microns. Contrary to theoretical analyses in the literature, our results reveal that the coefficient and exponent characterizing the advance of both the first front as well as the following unstable front is not a constant depending only on geometry (i.e. rectilinear vs axisymmetric spreading) but varies with the initial surfactant concentration of the deposition volume. Furthermore, the overall speed of the fronts is observed to increase with ambient relative humidity, an effect we ascribe to a reduction in the viscosity of the glycerol film due to absorption of water from the ambient atmosphere. Only in cases of relatively high humidity (higher than approximately 40% relative humidity) do we observe the formation of fractal patterns in the unstable front. Measurements of the fractal dimension yield values in the range 1.45-1.65. The largest values approximate those fractal dimensions observed in systems undergoing diffusion driven aggregation or viscous fingering, neither of which mechanism is pertinent to Marangoni flow.

Contents

List of Figures

1: Introduction

1.1 Literature Review

The conditions that enable a drop of liquid to spread on the surface of a second liquid were first stated by Carlo Marangoni in 1865. He ascribed the phenomena to surface tension and established the following law in an example of oil spreading on water:

> When the sum of the surface tensions of the upper and lower surfaces of the oil drops is less than the surface tension of the clear surface of the water, then the edges of the drops are pulled and they continue to enlarge. When on the other hand the aforementioned sum is larger than the surface tension of the underlying liquid, the drops remain stationary in the form of lenses. [25]

In other words, when one liquid is placed on another liquid and a sufficient surface tension gradient is present between the two liquids, the upper liquid will be induced to spontaneously spread on the underlying liquid. If a sufficient surface tension gradient is not present, the upper liquid will remain in a droplet form and not spread. Henceforth, the spontaneous spreading of one liquid on another liquid due to gradients in surface tension has been named Marangoni forces in honor of Carlo Marangoni's work on this topic. In future years it would also be discovered that instabilities would often form behind the initial front caused by Marangoni spreading.

The spreading of a surfactant solution on a thin liquid film was first discovered by Marmur and Lelah (1981) [26] to exhibit a peculiar instability at its advancing front, on what they assumed to be dry glass. Their observations showed that the sparingly soluble surfactant AOT spread uniformly and circularly at concentrations below the critical micelle concentration (cmc). However, spreading above the cmc was accompanied by "fingers" of surfactant originating near the point of drop deposition. Similar experiments were conducted by Wu, Troian and Safran (1989) [39] using aqueous AOT solutions on a water film ranging in thickness from 0.1 to 1.0 μm in a closed environment to control evaporation effects, through which they found that no instability developed on a completely dry

substrate, but that fingering occurred both above *and* below the cmc with the initial film thickness affecting the pattern wavelength. From this, the authors drew the conclusion that, since an underlying film and surface tension gradients were needed for the fingering instability to occur, Marangoni stresses were the responsible driving mechanism for the instability. Driven by gradients in surface tension due to surfactant concentration gradients at the air-liquid interface, the advancing front then breaks up into fingers which bifurcate and lead to highly non-uniform spreading as shown in Figure 1.1.

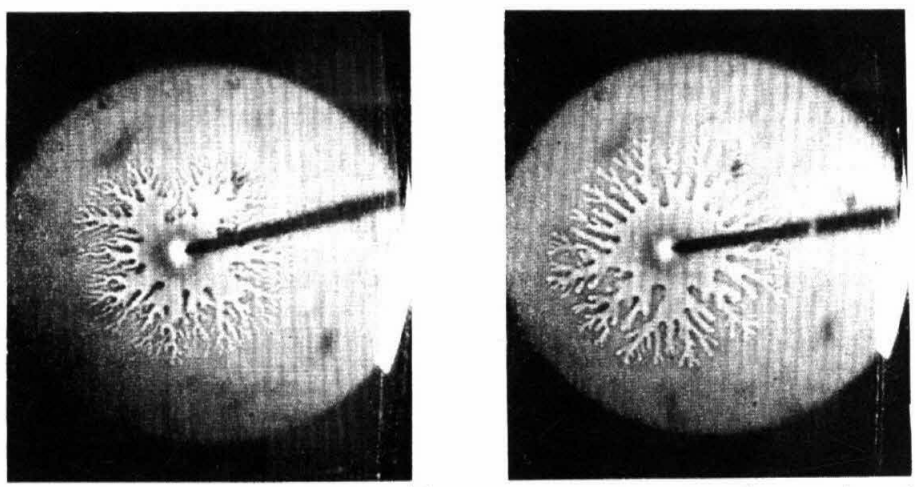

Figure 1.1: Photographs of an AOT droplet spreading and fingering. (a) Spreading on a thin water layer ($\approx 0.1\mu m$) and (b) spreading on a slightly thicker water layer ($\approx 1.0\mu m$). Image courtesy of Wu, Troian and Safran (1989) [39]

Frank and Garoff [11] [12] reported seeing "dendrites" when spreading ionic and non-ionic surfactant solutions on microscopically thin films in a vertical geometry, further confirming that fingered spreading cannot occur without the presence of both surface tension gradients and thin water films ahead of the spreading front. Narrow branching fingers were also observed when He and Ketterson [17] spread a monolayer of the insoluble ring-shaped surfactant valinomycin on a 1 μm water film on a vertical glass slide. Highly ramified fingering patterns were also seen when Darhuber, Fischer and Troian (2001) [7] placed a wire coated with a film of oleic acid on a 10 μm layer of glycerol on a silicon wafer, in which "streamlets" were observed in the thin region ahead of the oleic drop.

Herbolzheimer et al. (1989) [37] provided the first attempt at modeling the fingering instability of the spreading surfactant solutions in order to uncover the underlying mechanisms responsible. Exploiting the similarity between the patterns produced by spreading surfactant and those in the Hele-Shaw flow [40], their stability analysis allowed variation in surfactant concentration but not in film thickness, predicting the flow was unstable. This suggested the basic mechanism of the fingering to be, as with Hele-Shaw flow, due to an adverse mobility gradient. The greater layer height of the drop means it is more mobile than the adjacent thin areas. When the more mobile drop advances into less mobile areas with constant concentration gradient, infinitesimal protrusions advance faster than neighboring regions of the front, resulting in an unstable interface. However, more rigorous stability analyses performed by Matar and Troian (1997&1998) [27] [28] allowing disturbances in both film thickness and surfactant concentration reveal that the flow was stable to disturbances. Inclusion of weaker capillary and diffusion forces by Matar (1998) [32] confirmed the same result. A transient growth analysis was performed by Matar and Troian (1999) [29] [30] to study early time dynamics in the presence of Marangoni, capillary, and diffusion forces, which showed an explosive growth of disturbances in film thickness occurring in fractions of a second. The analysis also showed that disturbances of all wavelengths decay eventually. Matar and Troian (1999) [31] showed that in the presence of van der Waals forces, the amplification of initially small transverse disturbances was enhanced leading to sustained growth consistent with experimental patterns. The most recent work done on the theory of the instabilities is by Craster, Warner and Matar (2004) [23], who employed the transient growth analysis to reveal growth of linear disturbances. Inspection of the temporal evolution of the disturbance energy showed that after a short initial period of time, a perturbation of intermediate wavenumbers is selected. Decomposition of the instantaneous disturbance growth rate show that Marangoni stresses are primarily responsible for the instability, with capillarity and surface diffusion providing a large-wavenumber cut-off. Using transient growth analysis and direct numerical simulations of the two-dimensional lubrication equations, the authors were able to reveal disturbance growth, clearly showing the formation of fingers in the contact region behind the surfactant leading edge.

Aside from the theory, Afsar-Siddiqui, Luckham and Matar (2003) [3] attempted to classify these instabilities for film thicknesses between 25 to 100 μm, and found that the fingering instability is more likely to occur with decreasing film thickness and, in agreement with Troian, Wu and Safran (1989) [39], for increasing concentration up to the vicinity of the cmc.

The growth rate of the spreading surfactant front has also been under study for the past few decades. Troian, Wu and Safran (1989) [39] was the first to experimentally measure the growth rate of the unstable fingers, claiming a rate of $R \sim t^{\alpha}$, with $\alpha = 0.70$ and 0.66 for a 1.0 μm and 0.1 μm water film, respectively. Not long afterwards, Jensen and Grotberg (1992) [20] [14] solved the equations of motion in axisymmetric and planar geometries and found that the advancing front should advance according to $R \sim t^{\frac{1}{4}}$ for axisymmetric geometries and $R \sim t^{\frac{1}{3}}$ for planar geometries. The theoretical value for axisymmetric geometries has been confirmed experimentally by Dussaud, Matar and Troian (2005) [4], Afsar-Siddiqui, Luckham and Matar (2003) [3], and Fallest et al. (2010) [8] on film thicknesses ranging from 25 μm to 0.98 mm. However, Pereira (1995) [34] reports observing $R \sim t^{\frac{2}{3}}$ for film thicknesses of 0.1 mm, and $R \sim t^{0.57}$ for film thicknesses of 0.05 mm.

In this thesis, we present our experimental investigation of ultra-thin films, specifically 2.5 microns thick. We explore the parameter regime of altering concentration of the deposited surfactant, in an attempt to classify how the concentration of the deposited surfactant affects the spreading patterns as well as the speed of the advancing front. Additionally, we provide studies on the effect of ambient humidity on our experiments, through what we assume are changes in viscosity of the underlying film. We also study the effect of changing the deposited surfactant volume on the spreading dynamics. Finally, we present an investigation of the fractals and fractal dimensions that develop behind the first front.

1.2 Motivation

Why do we bother studying this? The spreading of a surfactant on a thin liquid film of higher surface tension is a process important to many household, industrial, and biomedical applications. Common examples of surfactants are soaps, shampoos, and detergents. Surfactants may also act as wetting agents, emulsifiers, foaming agents, and dispersants. Thus, surfactants are widely used in industrial processes. Specifically, the study of the spreading of surfactants is particularly crucial to processes such as lubrication and oil spill clean-ups.

Of biological and medical interest is the pulmonary surfactant. Neonatal respiratory distress syndrome is a disease occurring in infants whose lungs have not yet fully developed. Those suffering from this disease lack pulmonary surfactant in their lungs, a compound which would help the lungs inflate with air and keep the air sacs from collapsing. As treatment, doctors usually deliver artificial surfactant directly to the infant's lungs, but this is highly dangerous as scientists are still unsure as to how much surfactant should be administered. Additionally, the fact that surfactants tend to develop an instability when spreading on thin films presents a further complication since the surfactant might not uniformly coat the lungs once administered. Studying the spreading properties of these surfactants provides a step towards understanding how to treat this disease [2].

2: Background

In this chapter, some necessary background information relevant to this project will be summarized.

2.1 Surface tension, surfactants, and critical micelle concentration

Surface tension is defined as the force per unit length required to extend a liquid surface. Units of surface tension are typically in dynes per cm. A clean water-air interface has a surface tension of approximately 73 dyn/cm. A clean glycerol-air interface has a surface tension of approximately 64 dyn/cm.

A surfactant is a type of compound which, when added to water or a similar liquid, has the ability to reduce its surface tension. A surfactant molecule consists of a hydrophobic chain attached to a smaller hydrophilic head. When added to water, the hydrophobic tail tends to avoid the water, and hence the surfactant molecule escapes to the water-air interface. This subsequently decreases the surface tension of the interface. See Figure 2.1

As more surfactant is added to the solution and more molecules diffuse to the surface, the area of the water directly contacting the air decreases, causing the surface tension to decrease. Continued addition of the surfactant will eventually result in the surface being completely covered in surfactant molecules, at which point further addition of surfactant will not cause anymore surface concentration change, and hence the surface tension remains constant. Meanwhile in the interior of the water, the hydrophobic chains tend to avoid water, and the molecules form "micelles" by clustering together. Figure 2.2 shows a diagram as to what happens as more surfactant is added to water.

The point at which the surface is saturated with surfactant molecules and hence no more molecules can go to the surface is called the critical micelle concentration, or cmc. At this point, further addition of surfactant molecules are forced to form micelles in the bulk, and the surface tension remains constant with further addition of surfactant. The

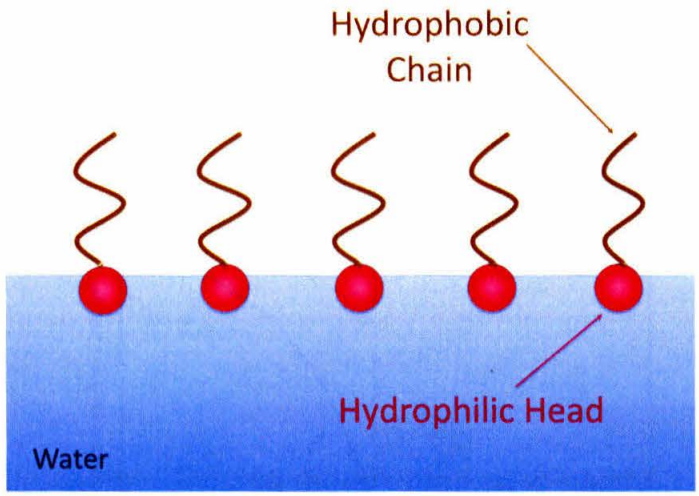

Figure 2.1: Surfactant molecules consist of a hydrophobic chain attached to a smaller hydrophilic head. When added to water, the hydrophobic tail tends to avoid the water, causing the surfactant molecules to escape to the water-air interface as shown here. This subsequently decreases the surface tension of the interface.

cmc varies between different surfactants. Relatively insoluble surfactants such as AOT have low cmcs because the molecules prefer not to form micelles at early times. On the other hand, relatively soluble surfactants such as SDS have higher cmcs because they do not mind forming micelles in the bulk of the liquid.

Surfactants can divide into two main categories depending on whether or not they ionize when added to water. Figure 2.3 summarizes this classification. In this experiment, we only work with the anionic surfactant AOT. This means that AOT, upon dissociation with water, has a negatively charged head.

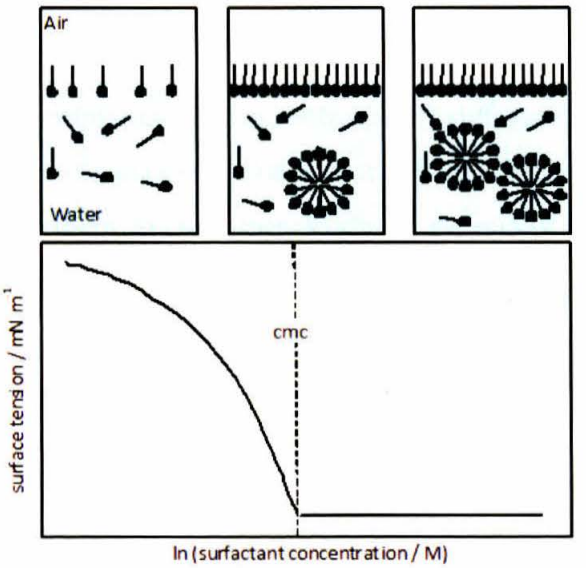

Figure 2.2: The top panel here gives a visual representation of the surfactant molecules in solution, while the bottom panel gives the corresponding surface tension measurements. Adding surfactant to a solution decreases the solution's surface tension. Continued addition of a surfactant will eventually result in the solution surface being saturated in surfactant molecules, at which point further addition of the surfactant will no longer cause any surface tension change. Image courtesy of [19]

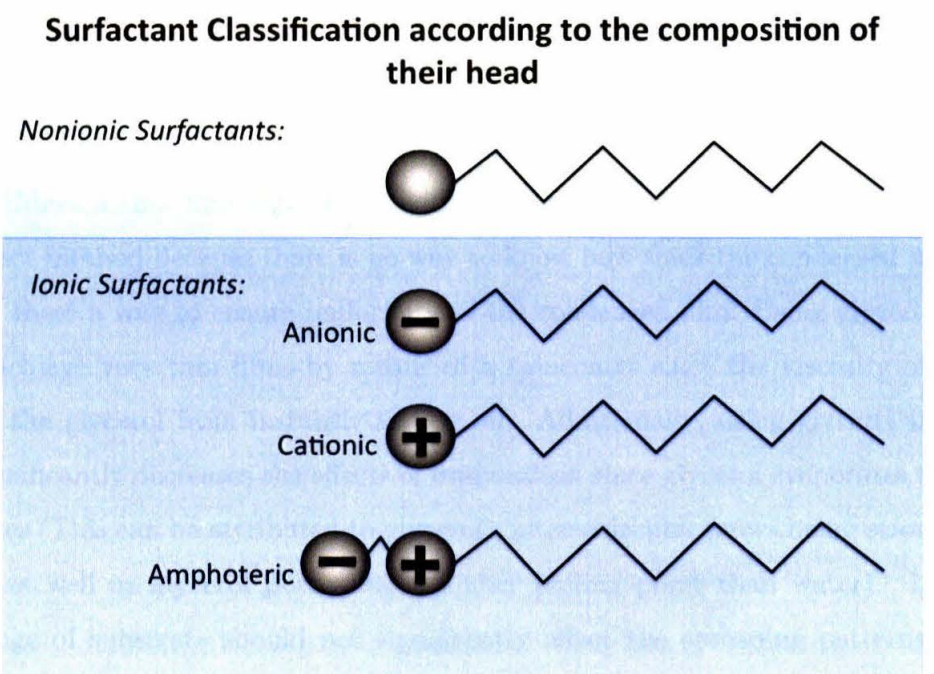

Figure 2.3: Surfactant classification according to the composition of their head: nonionic, anionic, cationic, amphoteric.

2.2 Dioctyl sodium sulfosuccinate (AOT)

The chemical name of this compound is Bis(2-ethylhexyl) sulfosuccinatesodium salt. It is also called dioctyl sodium sulfosuccinate, but is more often referred to as Aerosal OT or AOT. It is a common ingredient in consumer products, especially in laxatives as well as emulsifying, wetting, and dispersing agents. AOT was a component of the oil dispersant Corexit which was used in the Deepwater Horizon oil spill of 2010 [41].

AOT is an anionic surfactant, meaning it has a negatively charged head upon dissociation in water. Its formula weight is 444.56 g/mol. Its solubility in water is 8.17 g/l at 20 °C and 15 g/l at 25 °C, meaning it is relatively insoluble in water. Its solubility is better in less polar solvents, but it is relatively soluble in glycerol, although glycerol is a rather polar solvent. The cmc of this compound is rather ambiguous, reported as 0.68 mM [18] to 2-5 mM [1].

2.3 Glycerol

In this experiment, glycerol was chosen as the base film instead of water for a couple of reasons. In this thesis, we hoped to achieve analysis of the experiment on very thin films of the order of microns, which is difficult to achieve with water because the primary way to achieve a thin film with water is through condensation. Condensation is a very non-perfect method because there is no way to know how thick the condensed water film is, nor is there a way to ensure uniformity of the condensed film. Using glycerol, we are able to achieve very thin films by means of a spincoater since the viscosity of glycerol prevents the glycerol from instantly sliding off. Additionally, using glycerol instead of water significantly decreases the effects of evaporation since glycerol evaporates far slower than water (This can be attributed to glycerol's intermolecular forces being stronger than water's, as well as glycerol possessing a higher boiling point than water). In theory, this change of substrate should not significantly affect the spreading patterns because water and glycerol have very similar surface tensions (72.7 dyn/cm @ 68 °F for water, 63.4 dyn/cm @ 68 °F for glycerol). Glycerol and water do, however, have very different

viscosities (1.002 mPa s @ 68 °F for water, 1.069 Pa s @ 68 °F for glycerol) but theory says that in such thin films, the viscosity should not matter that much. We will show that this is untrue: viscosity does, in fact, strongly affect the spreading patterns.

2.4 Hygroscopic properties of glycerol

Glycerol has the property of being incredibly hygroscopic, meaning it readily absorbs water from the air. Upon exposure to air, glycerol will gain or lose moisture until it reaches a concentration that is in equilibrium with the surrounding atmosphere. This property ends up having very large consequences on the results of this experiment, since samples conducted in different humidities lead to different equilibrium water-absorption concentrations for underlying glycerol film. Specifically, on more humid days, there is more water in the air to be absorbed into the glycerol, so the film of glycerol ultimately has a higher water concentration than on a less-humid day. The curve in Figure 2.4 can be used to determine the relationship between relative humidity and the equilibrium concentration of glycerol. How soon this equilibrium is achieved depends on many factors. However, in relation to this experiment, the equilibrium should be achieved within a couple of minutes because the glycerol film is very thin. An experimental determination of the rate of equilibrium is presented in the Data section.

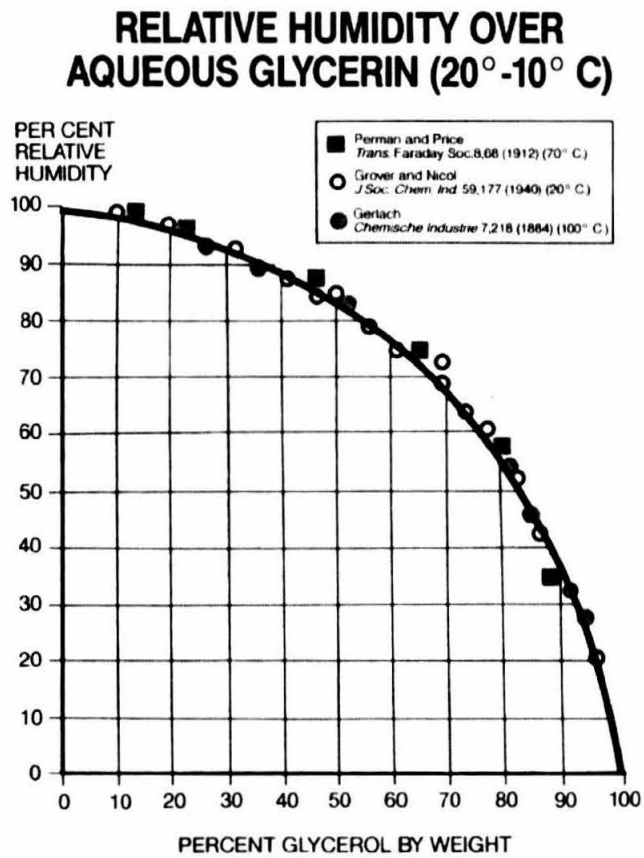

Figure 2.4: This graph can be used to determine the relationship between relative humidity and the equilibrium concentration of glycerol (and water), expressed as the percentage of glycerol held by an aqueous solution of glycerol when the transfer of water vapor between air and the glycerol solution is in balance. Image courtesy of [45]. The data on this graph is collapsed from references [35], [16], and [15]

2.5 Spreading driven by gradients in surface tension

A gradient in surface tension at an air-liquid interface results in a shear stress along the surface, which can cause flow. This surface tension gradient can be produced by either a gradient in temperature or a gradient in concentration. If σ denotes surface tension, T denotes temperature, c denotes concentration, and x the length,

$$\frac{d\sigma}{dx} = \frac{d\sigma}{dT}\frac{dT}{dx} \quad \text{or} \quad \frac{d\sigma}{dx} = \frac{d\sigma}{dc}\frac{dc}{dx}. \tag{2.1}$$

Gradients in surface concentration are obtained when a drop of surfactant is placed on a clean water surface because of the mobility of surfactant molecules and their tendency

to escape to the surface. Initially, there is no surfactant on the water surface. When a drop of surfactant solution is gently placed on the water, the concentration of surfactant is naturally greatest at the edge of the drop. Then as the molecules start to spread along the surface, the number of surfactant molecules further away from the drop will be less than those in the vicinity of of the drop, and hence a gradient in the number of molecules results, as demonstrated in Figure 2.5. This concentration gradient inherently results in a surface tension gradient, which drives flow. Flows caused by gradients in surface tension (due to either temperature or concentration) are often called Marangoni flows in honor of Marangoni who first described such flows in 1865.

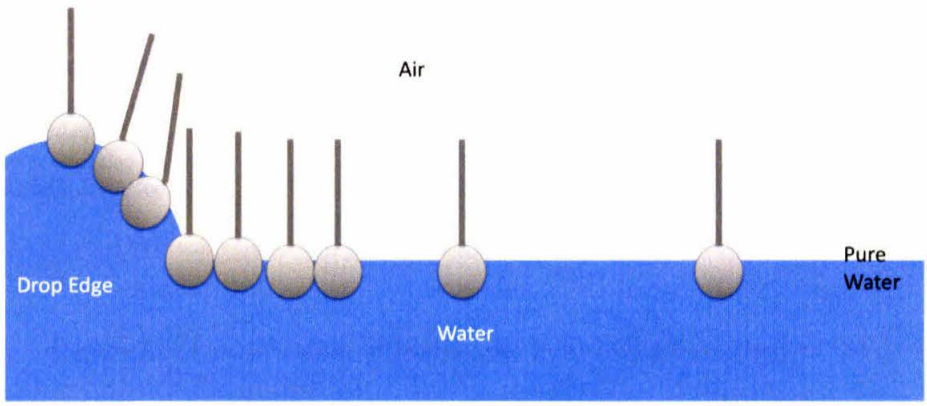

Figure 2.5: The concentration gradient that is established when surfactant is deposited on a water film.

2.6 Marangoni instabilities

Marangoni flows can be either stable or unstable, and the instabilities inherent in unstable flows are referred to as Marangoni instabilities. Figure 2.6 is a general framework identifying the frameworks under which these systems can be classified.

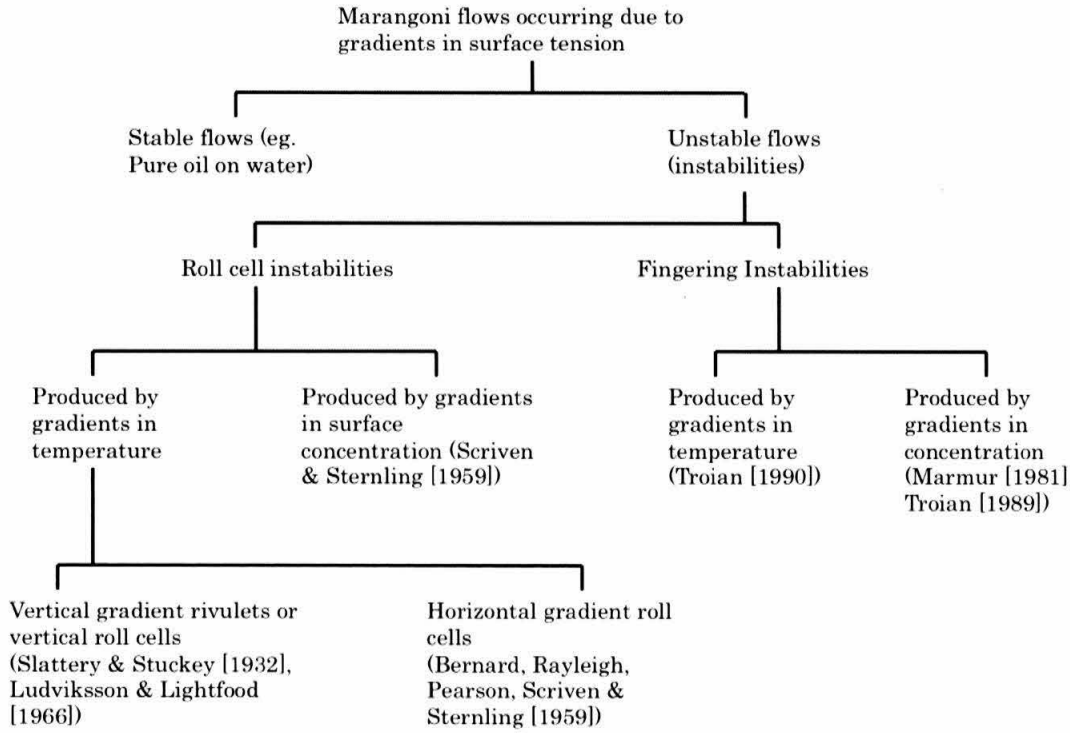

Figure 2.6: Classification of Marangoni flows. Chart courtesy of [34].

2.7 Fractal Dimensions

Fractals are relevant to this project because we find the spreading patterns to be surprisingly fractal-like. For this reason, the fractal dimension is a relevant parameter to study for this project.

Mathematician Benoit Mandelbrot first coined the term *fractal* in 1975. A fractal is a mathematical set that typically displays self-similar patterns across many different scales [24]. Fractal patterns are very familiar to us, since nature is full of fractals. For example: trees, rivers, coastlines, mountains, clouds, seashells, hurricanes, etc, are examples of the many instances of fractals found in nature. Fractals can also be used to characterize such phenomena as turbulence, urban growth, and market trends.

A fractal dimension provides information on how complex a fractal is. The fractal

(a) Romanesco Broccoli. Fractal Dimension ≈ 2.66.

(b) Coast of Norway. Fractal Dimension ≈ 1.52.

(c) Juniper Leaves. Fractal Dimension ≈ 1.79.

Figure 2.7: Examples of fractals in nature.

dimension is defined as the ratio of the change in detail to the change in scale. Fractal dimensions can be thought of as an extension of topological dimensions– 1 is used for sets describing lines, 2 for sets describing surfaces, and 3 for sets describing volumes. However, unlike topological dimensions, the fractal index can take on non-integer values, indicating that these sets fill space differently from ordinary geometrical sets. For example, a curve with a fractal dimension of 1.1 would behave similarly to an ordinary line since its fractal dimension is near 1. But a curve with fractal dimension of 1.9, for example, would wind convolutedly through space, nearly filling an area. Its fractal dimension, very close to 2, indicates that this curve behaves almost like a surface.

The fractal dimension of a curve can be calculated in a couple of different manners. For the purposes of this thesis, we will only cover the logistics of how to calculate the fractal dimension using the *ruler method*. In this method, the fractal dimension is defined as

$$D = \frac{\log(\text{number of self-similar pieces})}{\log(\text{magnification factor})} \tag{2.2}$$

For an example of how to calculate the fractal dimension using the Ruler Method, take a look at Figure 2.8. The figures shown in this image are called the Koch Curve. The first figure has a ruler size of 1/3, and the curve has 4 self similar pieces. The second figure has a ruler size of 1/9 and 16 self similar pieces. The third figure has a ruler size of 1/27 and 64 self similar pieces. When we plug these numbers into the equation for fractal

dimension, we calculate a dimension of approximately 1.26 for all the images. The fractal dimension of the Koch curve is generally agreed to be 1.26.

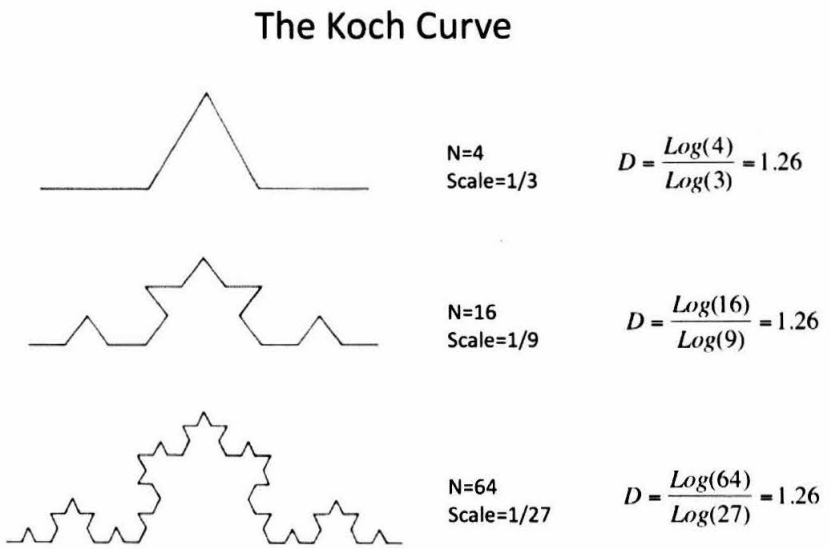

Figure 2.8: Calculating the fractal dimension for the Koch Curve.

2.8 Spreading Pressure Pi

An important value to look at in these experiments is the spreading pressure, which we will call Π. This value is defined as $\Pi = (\sigma_{liquidsubstrate} - \sigma_{surfactant})$, where $\sigma_{liquidsubstrate}$ is the surface tension of the underlying liquid substrate and $\sigma_{surfactant}$ is the surface tension of the surfactant droplet which is placed upon the underlying liquid substrate. For my experiment, pure glycerol was always the underlying liquid substrate. The surface tension of pure glycerol is approximately 64 dyn/cm. The surface tension of the droplet varied from sample to sample, depending on what concentration of AOT was used. The spreading coefficient is important because it is said to rule whether or not the surfactant spreads, as Marangoni famously reported in 1865 [25]. Additionally, the spreading coefficient is said to govern the speed of the spreading surfactant, the details of which are covered in the next section: The Model.

2.9 The Model

We consider an incompressible, Newtonian film of uniform thickness H_0^*, viscosity μ^*, and density ρ^* supported by a flat rigid substrate at $y^* = 0$. Initially, the liquid surface is only partly covered by the insoluble surfactant whose surface concentration Γ^* achieves its maximum value Γ_m^* at the origin $x^* = 0$ and smoothly vanishes at $x^* = L_0^*$. The surface tension corresponding to Γ_m^* is denoted by σ_m^* while σ_0^* corresponds to the surface tension of the uncontaminated liquid surface. The equations of motion are derived in the lubrication approximation for which $\epsilon = H_0^*/L_0^* \ll 1$. The surfactant and underlying fluid spontaneously spread toward the contaminated region as a result of the initial gradient in surface tension characterized by $\Pi^*/L_0^* = (\sigma_0^* - \sigma_m^*)/L_0^*$, where Π^* is the spreading pressure. This flow is counter-balanced by the viscous stress at the surface which is of order $\mu^* U^*/H_0^*$. The spreading velocity characteristic of Marangoni driven flow in thin films is determined from this tangential stress balance to be $U^* = \epsilon\Pi^*/\mu^*$.

The equations are then reduced to dimensionless form by introducing characteristic scales relevant to the dynamics of a thin liquid film driven to spread by Marangoni stresses. The horizontal coordinates x^* and y^* are scaled by the length of the initial surfactant strip, L_0^*; the vertical coordinate y^* is scaled by the initial film thickness H_0^*. Within the lubrication approximation, the axial and transverse velocities u^* and w^* are scaled by U^* while the vertical velocity v^* is scaled by ϵU^*. The characteristic time scale is given by L_0^*/U^* and the local surface concentration and surface tension are normalized by their values at the origin, namely Γ_m^* and σ_m^*. Likewise, the local driving force for spreading is normalized by Π^*.

Since both the Reynolds number ($Re \equiv (\rho^* U^* H_0^*)/\mu^*$) and ϵ are vanishingly small in this system, the inertial terms in the Navier Stokes equation can be ignored. For sufficiently thin films as applicable in this thesis, the Bond number ($Bo \equiv \rho^* g^* H_0^{*2}/\Pi^*$) is also negligible. There are three relevant dimensionless numbers appearing in the equations of motion which reflect the importance of surface curvature, surface diffusion (represented by the diffusion coefficient D_s^*), and van der Waals forces. These numbers are defined by an in-

verse modified capillary number, $C \equiv \epsilon^2 \sigma_m^* / \Pi^*$, a surface Peclet number $Pe_s \equiv U^* L_0^* / D_s^*$ and a modified Hamaker constant $A \equiv \widetilde{A} / 6\pi \Pi H_0^{*2}$. The two coupled equations describing the spatio-temporal evolution of the film thickness and surfactant concentration are defined by Equations 2.3 and 2.4 below. Complete details of the derivation leading to these differential equations have been skipped in this discussion, but can be found elsewhere [14] [20] [32].

$$H_t + \frac{1}{2}\nabla \bullet (H^2 \nabla \sigma) + \frac{C}{3}\nabla \bullet (H^3 \nabla^3 H) + A\nabla \bullet (\frac{1}{H}\nabla H) = 0, \tag{2.3}$$

$$\Gamma_t + \nabla \bullet (H\Gamma \nabla \sigma) + \frac{C}{2}\nabla \bullet (\Gamma H^2 \nabla^3 H) + \frac{3}{2}A\nabla \bullet (\frac{\Gamma}{H^2}\nabla H) = \frac{1}{Pe_s}\nabla^2 \Gamma. \tag{2.4}$$

The first equation represents fluid mass conservation, and the second equation represents surfactant conservation. These equations are coupled by the surfactant equation of state which relates the surface tension to the local surfactant concentration. This entire section is from Matar and Troian (1999) [31].

2.10 Velocity profiles and variation of spreading distance with time

Jensen and Grotberg [20] derive the axisymmetric spreading exponent of a surfactant on a film using simple scaling arguments. They show that the radius of a spreading front of insoluble surfactant from a finite source spreads in time as a power law, or $t^{\frac{1}{4}}$ for the case of Marangoni dominated spreading. The Marangoni stress balance at the air-liquid interface is given by

$$\frac{\partial \sigma}{\partial r} = \frac{\partial u}{\partial z}, \tag{2.5}$$

where σ is the local surface tension, u is the tangential velocity, and μ is the film viscosity. A simple scaling of the above equation gives

$$\frac{\Pi}{R} \sim \mu \frac{U}{H_0}, \tag{2.6}$$

in which R denotes the radial extent of the drop, U is a characteristic velocity, and H_0 is the initial film thickness. The spreading pressure, Π, is given by the difference in

surface tension between the surfactant drop and the film ahead:

$$\Pi = \sigma_0 - \sigma_m. \tag{2.7}$$

Expressing surface tension as a function of surfactant concentration, Γ :

$$\sigma = \sigma_0 - \alpha\Gamma, \tag{2.8}$$

where α denotes surfactant activity. (Note that although we approximate surface tension to be a linear relationship with surfactant concentration, actual measurements of surface tension do NOT typically follow such a linear relation except in a limited range for very dilute concentrations.) We next define the total mass of the surfactant in the spreading drop, M, as

$$M = \int_0^\infty 2\pi r\Gamma dr \sim R^2\Gamma_m. \tag{2.9}$$

After substitutions and rearrangements, we arrive at

$$R^4 \sim \frac{4\alpha M H_0}{\mu}t, \tag{2.10}$$

so that the following power-law relation for Marangoni-driven spreading is obtained:

$$R \sim t^{1/4}. \tag{2.11}$$

This derivation assumes that the surfactant is spreading from a finite source. A possibly more correct assumption is that the surfactant acts like an infinite reservoir, since surfactants are capable of covering far more area than the chip allows. Hence, if we use an infinite reservoir approximation and do not make the substitution shown in Equation 2.9 for mass, we arrive at the following:

$$R^2 \sim \frac{4\alpha M H_0}{\mu}t, \tag{2.12}$$

or that

$$R \sim t^{1/2}. \tag{2.13}$$

2.11 Goals

There has been over a decade of theory regarding this topic, with very few experiments. This thesis aims to ground the theory by classifying the dynamics of how surfactants distribute on a thin film in terms of velocity of the moving fronts, as well as the fingering tendencies and fractal dimensions of the fingering front. The surfactant studied in this project was dioctyl sodium sulfosuccinate (AOT). This regime of ultra-thin films has had very little experimental research associated with it, particularly because ultra-thin films are difficult to achieve with water. This regime is, however, incredibly important because this regime is particularly applicable to biology.

3: Experimental Setup

The experimental setup used to visualize and record the spreading patterns was set up as shown in Figure 3.1. This entire set-up was on top of a Newport Vision Isostation optical table for the purposes of reducing movement in the system as well as ensuring that the system and samples were level.

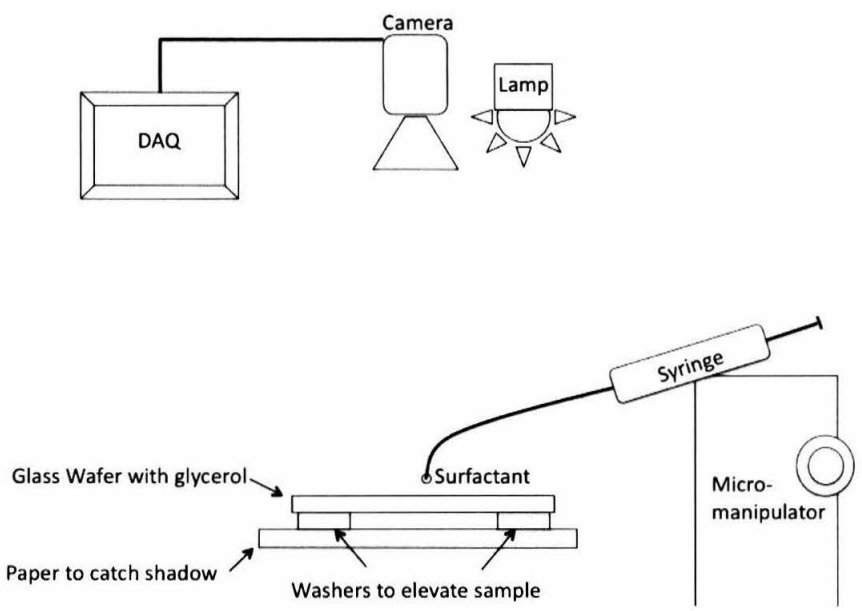

Figure 3.1: The experimental setup.

3.1 Components

The components listed below were used for all reported experiments unless otherwise specified (these components were not used in the Volume differences section).

3.1.1 Micromanipulator

A micromanipulator was constructed by stacking three translation stages in such a way that each knob enabled the entire contraption to move in a different x-, y-, or z- direction.

This was necessary to ensure a controlled deposition of the surfactant droplet from the syringe, which was attached to the micromanipulator.

3.1.2 Syringe

The syringe used was a Hamilton SYR 50 μL syringe, product 1705 TLL-XL. Its termination was a PTFE Luer Lock, which can attach to the flexible tubing we used: Hamilton KF22TF Tubing Assay 22 gauge, 1 foot length. This tubing was stabilized by a rod protruding from the micromanipulator. The flexible tubing was used because it enabled us to bend it in such a way that the end of the tubing was vertical. This way, the droplet deposited from the tubing hung vertically and hence symmetrically for an even droplet deposition.

3.1.3 Glass Wafer

The glass wafers used were Edmund Optics (product 44063) float glass circular window wafers, 51.5 mm in diameter and 1.5 mm thick. We found that this size of wafer did not hinder the spreading process, as the spreading surfactants did not reach the ends of the wafer, but rather stopped a couple of millimeters before the edge. Additionally, the axisymmetry of the circular wafer ensured that the surface gradients experienced by the surfactant droplet were also axisymmetric.

3.1.4 Projection screen

The paper used for imaging was a simple piece of white printer paper taped to the table. Its entire purpose was to catch the shadow cast by the spreading droplet. A 2.5cm x 2.5cm square was sketched in pencil onto this paper to help the user visualize where the field of the camera resided.

3.1.5 Washers

Washers were used to prop the wafer up at a distance above the imaging paper such that an appropriate shadow could be cast from the sample onto the imaging paper. The thicknesses of the wafer were intentional as this thickness allowed for the ideal shadows

to be cast: at this thickness, there was an ideal balance between thickness and crispness of the shadows. The washers were 2.5 mm thick and 1.6 cm in diameter. There were four washers, each positioned at a corner of the square sketched onto the printer paper. All washers were in direct contact with the glass wafer and the projection screen.

3.1.6 Lamp

A Fostec 8375 150 Watt optical fiber lamp was used. The beam was sent through a diffuser also supplied by the manufacturer. The head of the beam was positioned approximately 40 cm above the projection screen, positioned with respect to the camera in a fashion such that the camera did not cast a shadow on the viewing area and also the lamp head did not interfere with the field of view of the camera. Additionally, adjustments were made so that the camera did not capture a glare from the lamp reflected in the glass wafer. Ideally, the lamp was nearly perfectly above the sample so that the shadows cast from the sample onto the paper were uniform across the chip.

3.1.7 Camera

An ace Series acA2500-14 um video camera from Basler was used, with resolution 2592 x 1944. Its maximal frame rate was reported at 14 frames per second (fps), although we found that we were able to achieve 15 fps rates with no loss of quality. The camera was a monochrome GigE video camera, positioned approximately 20 cm above the projection screen. Attached to its lens was a 35 mm high resolution fixed focal length lens from Edmund Optics, for focusing purposes. The lens was adjusted so that the projection screen (and not the glass wafer) was at the depth of focus, because the projection screen contained the shadows that we were imaging.

3.1.8 DAQ

The video camera settings were first adjusted via the Matlab 2013a built-in program `imaqtool` to optimize the image quality. Usually, the only setting to be adjusted was the "Exposure Mode" setting, which we set at "Once" so that the exposure was optimized once at the beginning and then kept constant for the rest of the video. The output signal

from the video camera was then recorded on the laboratory computer using a program we wrote in Matlab R2013a. This program took a video for seven seconds straight at 15 fps and stored it on the computer.

3.2 Experimental Procedures

I will provide a brief summary of the experimental procedures associated with each sample taken. The first step was cleaning off the glass wafers. This was done by soaking the wafers for at least thirty minutes in a piranha etch (a 3:1 ratio of sulfuric acid to hydrogen peroxide). The wafers were then soaked briefly in deionized water (approximately 5 seconds) and then rinsed off with a squirt bottle of deionized water. (This rinsing process was found to be necessary because during the soaking process, a thin film of impurities would form on the chip. Without the rinsing, the film would cause the glycerol to dewet on the wafer. Rinsing with water removed the film and allowed the glycerol to completely wet the wafer). Next, the bottom of the wafer was gently dried with a TechniCloth wipe, and the wafer then placed on the spin coater. The wafer was then spun at 10,000 rotations per minute (RPM) for approximately 20 seconds until the wafer was completely dry of water. Next, approximately 1 mL of glycerol was gently and slowly deposited onto the wafer using a plastic syringe such that bubbles did not form in the glycerol. Then the wafer was spun at 10,000 RPM for 120 seconds. Using the following equation derived by Emslie, Bonner and Peck (1958) [5], we were able to then determine the height of the spun film:

$$h = \frac{h_0}{(1 + 4Kh_0^2 t)^{\frac{1}{2}}} \text{ , where } K = \rho\omega^3/3\eta. \tag{3.1}$$

(In this equation, h_0 corresponds to the initial height of a fluid layer, ρ is the density of the liquid, ω is the angular velocity at which the disk is spun, η is the viscosity of the liquid (here glycerol), and t is the time for which the disk is spun. We predicted h_0 by dividing the volume of the deposited glycerol by the area of the wafer. Although this number is only a rough estimate of the real initial height, this ends up not being important at the times and speeds we are spinning at.)

Using this equation, our films are predicted at a thickness of approximately 2.5 μm.

Visually, at a certain angle, one can see the film of glycerol on the chip catching the light (due to the interference of light). This film was purple in color from the correct angle. At all other angles, the film was clear and colorless. The wafer was then transferred to the imaging room and placed under the camera. This transfer process took approximately 10 seconds. Then the syringe (with the preloaded 1.0 μL of surfactant solution) was positioned above the wafer and the surfactant squeezed out so that it dangled as a droplet from the needle or tubing. Then the video was prompted to begin recording, and the syringe was slowly lowered until the droplet contacted the film and spontaneously spread. The elapsed time between removing the chip from the spincoater and the surfactant coming in contact with the film was nearly always between 40 and 60 seconds.

3.3 Visualization of spreading drop

A visualization problem is evident considering the experiment is a transparent surfactant spreading on a transparent substrate (glycerol) on a transparent glass wafer. The solution to navigate this problem was to take advantage of the height differentials that arise during the surfactant spreading process. Image 3.2 gives a theoretical schematic of the height profile for a drop of surfactant spreading on a pure liquid film.

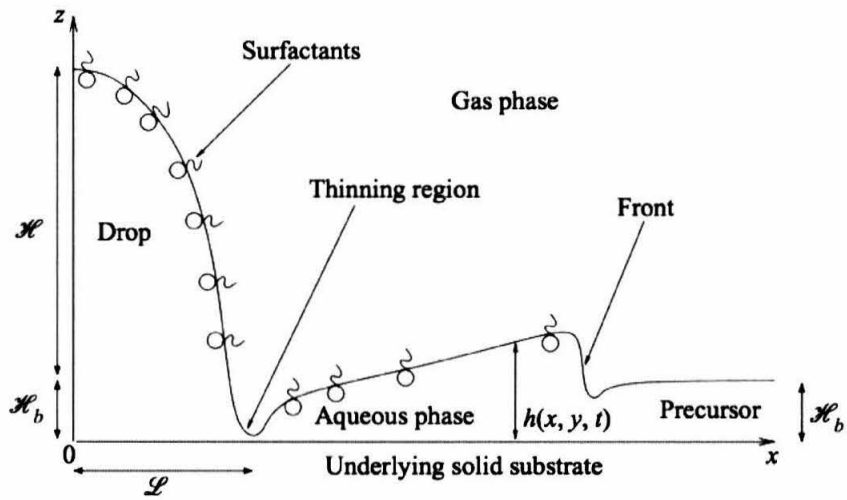

Figure 3.2: Schematic representation of the spreading of deposited surfactant over a thin liquid film. Image courtesy of [23].

Thus, using a lamp positioned above the experiment and a piece of white printer paper

positioned below the experiment, we cast a shadow from the spreading surfactant onto the white printer paper, which we then captured on a video camera. Although the details of which areas and which heights cast the specific shadows is not entirely clear, I do know that these shadows were visible because of the differing heights of glycerol and/or surfactant that the light had to travel through before hitting the paper.

3.4 Cleaning of labware

In between every sample, the flexible tubing on the syringe was thoroughly rinsed with a fresh beaker of deionized water from Millipore's MilliQ dispenser, and then thoroughly dried by pumping air through it. A Becton-Dickenson 5 mL Luer-Lok Tip Syringe was used for this cleaning process so that the air and water could be vigorously pumped through the tubing. We used the disposable BD syringe rather than the experimental syringe for this cleaning process as to not wear down the plunger seal on the significantly more expensive experimental syringe. Note there was no need to clean the experimental syringe because the amount (1.0 μL) of surfactant we used never reached the syringe– it was only enough to reach a couple of centimeters up the 1-foot length of flexible tubing.

At the end of every experimental wetlab day, the spincoater was thoroughly wiped down with acetone and then isopropyl alcohol. The glass wafers were roughly cleaned at the end of each experimental day by wiping them down with acetone. At the beginning of every experimental day, the glass wafers were thoroughly cleaned by soaking the wafers for at least thirty minutes in a piranha etch (a 3:1 ratio of sulfuric acid to hydrogen peroxide). The wafers were then soaked briefly in water (approximately 5 seconds) and then rinsed off with a squirt bottle of deionized water before continuing on with the rest of the experiment, as discussed in the section Experimental Procedures.

3.5 Preparation of surfactant solutions

As a reminder, molarity is defined as:

$$\text{Molarity (M)} = \frac{\text{moles solute}}{\text{liters solution}}. \tag{3.2}$$

AOT is a white wax-like solid, and was measured out using the Mettler Toledo AT20 electronic balance of 0.01 mg precision on Fisher weighing paper. The AOT was from Sigma-Aldrich, 98% pure Dioctyl sulfosuccinate sodium salt. The ultra pure deionized water was from Millipore's MilliQ dispenser, and the glycerol was from Macron Fine Chemicals (> 99.5% ACS).

Before preparing the solutions, we cleaned the containers and equipment associated with the preparation process. The new sample vials of 4 mL (from National Scientific Company) with provided teflon lids were rinsed with deionized water and then aired down with a nitrogen air gun and set aside. The spatulas were cleaned with water, then acetone and isopropyl alcohol.

Firstly a relatively large sample of three-to-one ratio of water-to-glycerol by volume was prepared by weighing appropriately-proportioned samples of the water and glycerol and then shaking them vigorously in the same container.[1] This aqueous glycerol solution was then measured into the 4 mL samples vials by weight using the electronic scale. Then specified amounts of the AOT were measured out on the scale, added to the vial, and the vial vigorously shaken until the salt dissolved. At this point, the solution would foam at the surface, but when left aside the bubbles would subside giving a clear solution.

Below is a summary of the solutions prepared that were used in this experiment. The molar mass of AOT is 444.56 g/mol, the density of water is 1.00 g/cm^3 and the density of glycerol is 1.26 g/cm^3. Hence, to calculate the molarity of a prepared solution using a three-to-one ratio of water-to-glycerol, we use:

$$\text{Molarity (M)} = \frac{\text{mass of surfactant (mg) } *1/(444.56 \text{ g/mol})}{(\text{mass solvent (g)})(\frac{0.75}{1g/cm^3} + \frac{0.25}{1.26g/cm^3})}. \tag{3.3}$$

[1] We chose this ratio of water-to-glycerol as our solvent because of trial and error. Many combinations for solvent had been tested prior to the results reported in this thesis, and we found that pure water spread too quickly for a camera to appropriately capture, yet demonstrated beautiful fractals. Pure glycerol, on the other hand, spread incredibly slowly (on the order of 20 minutes) yet did not exhibit fractal-like spreading, likely because the speed of the advancing front was too slow to bifurcate its instabilities. This three-to-one ratio of water-to-glycerol presented an appropriate balance between speed of fingers as well as fractal-like images.

Here is the data on the surfactant solutions we prepared: (using 75% water and 25% glycerol by volume):

Mass AOT used (mg)	0.26	2.368	2.72	3.494	4.128	6.72	10.50	14.10
Mass aqueous glycerol used (g)	4.002	4.258	4.097	4.253	4.259	3.998	3.995	4.052
Concentration AOT (mM)	**0.15**	**1.29**	**1.50**	**1.95**	**2.30**	**3.78**	**5.91**	**7.83**

3.6 Surface Tension Measurements

The surface tension measurements of the surfactant solutions were conducted using the pendant drop method. The pendant drop method is commonly used to measure the surface tension of liquids. It involves analyzing the shape of a drop hanging from a capillary tube and about to detach, which is very sensitive to the interfacial tension. A discussion of the analysis and physics of the pendant drop method can be found in the manual for the Pendant Drop ImageJ program [9].

The program used in this thesis to analyze surface tensions was the `Goutte_pendante` plug-in for ImageJ [36], which provides a tool to match a theoretical profile to the contour of a pendant drop. Although the drop profile is described only by one non-dimensional parameter (tip radius over capillary length), in practice multiple dimensional parameters can be adjusted using this plug-in: tip position and curvature, tilt of symmetry axis, and capillary length [9]. The surface tension can then be calculated from the capillary length as well as the density difference between the drop and the surrounding air.

The plug-in runs on a high contrast image of a pendant drop, obtained by taking a picture of the drop in front of a light source in the background, far away from the drop.

The image is then loaded into ImageJ and a rectangular region of interest drawn around the free surface of the drop. The parameters are then fitted and adjusted until the red outline fit produced by the plug-in fits the outline of the drop very nearly perfectly, similar to Figure 3.3.

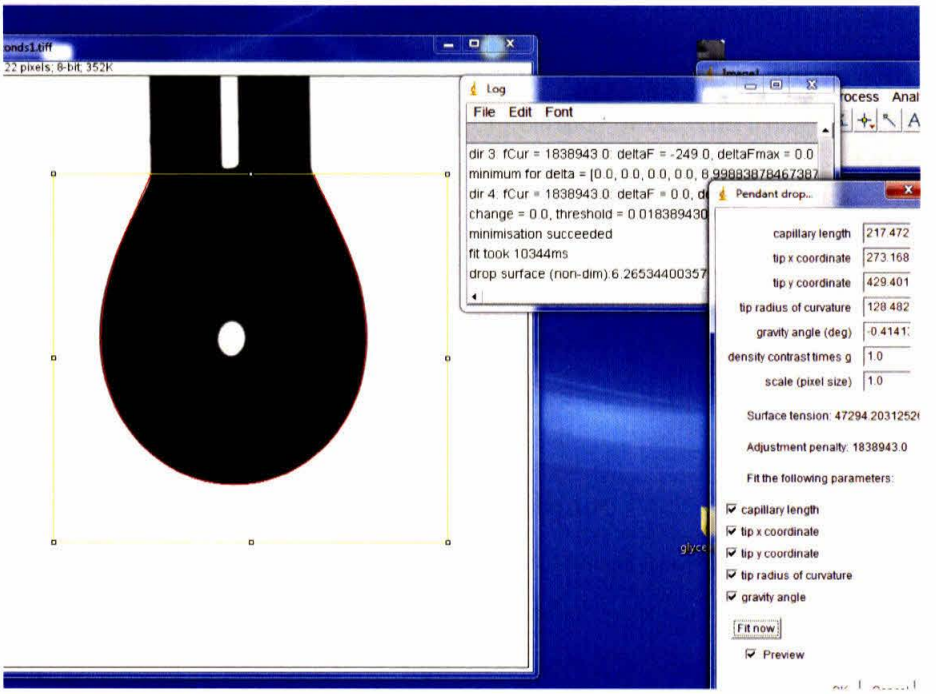

Figure 3.3: Pendant Drop program in ImageJ.

The surface tension of the droplet can then be calculated by the formula $\sigma = \Delta\rho g \ell_c^2$, where $\Delta\rho$ is the difference in density between the inside and the outside of the drop, g is gravitational acceleration, and ℓ_c is the capillary length produced by the plug-in, making sure to match all units and scales [9]. Specifically, the default capillary length produced by the plug-in is in units of pixels, which should to be converted to units the user prefers.

3.7 Image Analysis

Image analysis was done in Matlab 2013a, using code I wrote (as well as some that Kevin wrote). The frame rate was set to 15 fps, and a video set to capture for seven seconds straight. Afterwards, the frames were all extracted from the video so that each frame was its own picture to analyze. The image captured on the camera was then processed so that we could perform measurements on it. The end goal of the image processing was to have

an outline corresponding to the front we were trying to analyze.

We used images comprised of shadows that we captured on our camera, examples of which are shown in Figures 3.4(a) and 3.8(a). The image processing first involved subtracting off the background to eliminate lighting gradients, imperfections on the projection paper, etc. The background image was pulled from an early time in the video, at which point the surfactant had not yet been deposited. Next, the image was thresholded to a binary image, using parameters that optimized the continuity of the outline. The binary image was then cleaned up using functions in Matlab's Image Processing Toolbox `bwmorph`. Next, Sobel Edge Detection was used to find the edge corresponding to the front, and then the resulting image was again cleaned up using `bwmorph`. All of these steps just listed were automated using a program I wrote in Matlab. Examples of the resulting images can be seen in Figure 3.4(b) and 3.5(b). The image was then opened in Microsoft Paint, and the relevant area filled in with the Paint Bucket (see Figure 3.4(c) and 3.5(c)) after further minor patching of the outline, if necessary. The image was then opened again in Matlab, and another program used to pick out the colored pixels 3.4(d) and 3.5(d). This final image was of the quality needed to perform measurements.

One of the necessary measurements to be made was the radius of the advancing fronts. The definition of this radius is a bit open to interpretation because the front is not a perfect circle. A couple of options of the definition of the circle include the a) average radius of the points or b) the minimum encompassing circle of all the points. Because the unstable front in particular is incredibly non-circular, and also because the "average" radius of the points on such a complicated front holds little meaning, we have defined the radius to be the radius of the smallest encompassing circle of all the points.

The method used to find the minimum encompassing circle is similar to that used by Shamos and Hoey [42], taking advantage of the fact that the center of the smallest encompassing circle must be a vertex of the farthest-point Voronoi diagram of the input point set, or in our case, the boundary points. What our code does is first choose a

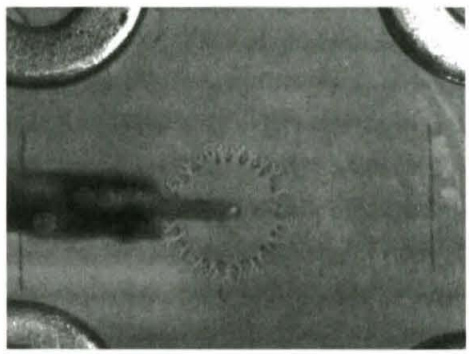

(a) The original image captured on the camera.

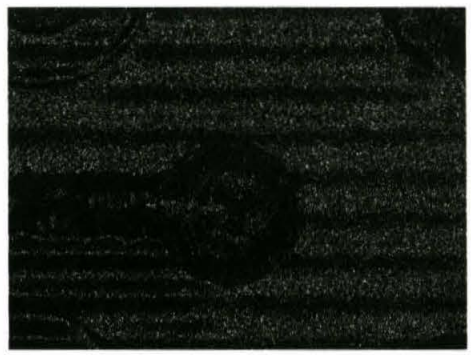

(b) After subtracting off the background, thresholding, edge detection, and clean-up.

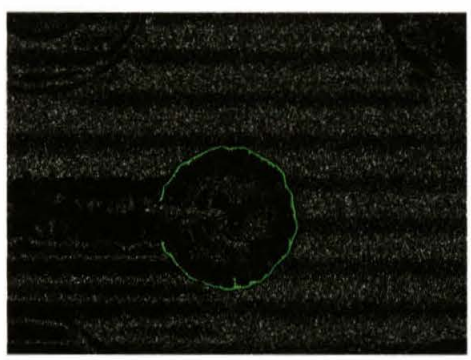

(c) The relevant area is filled in with Paint.

(d) This final image is of the quality needed to perform measurements.

Figure 3.4: Image Processing Steps for First Front Detection.

region of points that may contain the center (the middle third of points contained in the boundary). It then cycles through all those potential points, and for each point, finds the maximum distance from that point to any point on the boundary. This maximum is stored for each point. After each point has been cycled through, these maximum values are compared, to find the minimum value among the "maximum distances." The point that this value belongs to, is the center of the circle, and the value is the radius. Figure 3.6 is an example of the minimum encompassing circle and its center (in red) drawn onto the "first front" of which is being measured. Figure 3.7 is an example of the minimum encompassing circle and its center (in red) drawn onto the "unstable front" of which is being measured.

Another measurement that we made was the fractal dimension of the unstable front. The "Ruler method" used for measuring fractal dimensions has been discussed in the Background section. What our code does is first prompt the user to cut out the section of

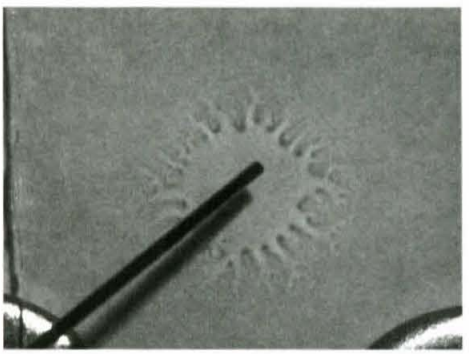

(a) The original image captured on the camera.

(b) After subtracting off the background, thresholding, edge detection, and clean-up.

(c) The relevant area is filled in with Paint.

(d) This final image is of the quality needed to perform measurements.

Figure 3.5: Image Processing Steps for Unstable Front Detection.

the outline containing the syringe needle since that area of the outline is blocked by the syringe and hence not visible. The starting and endings points of the measurements are then on either side of the removed needle. Next, the program determines a range of ruler sizes to use in the method. This is a rather important specification, because we want to be in a range relevant to the fractal-like features on our outline. If we go too small, we are measuring the flaws on the outline. If we go too large, we are no longer able to see the features we are trying to capture. Hence, the relevant fractal range was determined to be approximately one-sixth to one-third the radius of the minimum encompassing circle. The program then loops through every possible ruler size in the range, and then plots ruler size versus number of steps taken. On a log-log plot, the slope of the best-fit line is the fractal dimension. Figure 3.8 gives an example of the output of the program. In the top panel is the image, the outline in green and the "relevant" outline (meaning the needle is cut out) in red. On the bottom panel is the log-log plot of ruler size versus

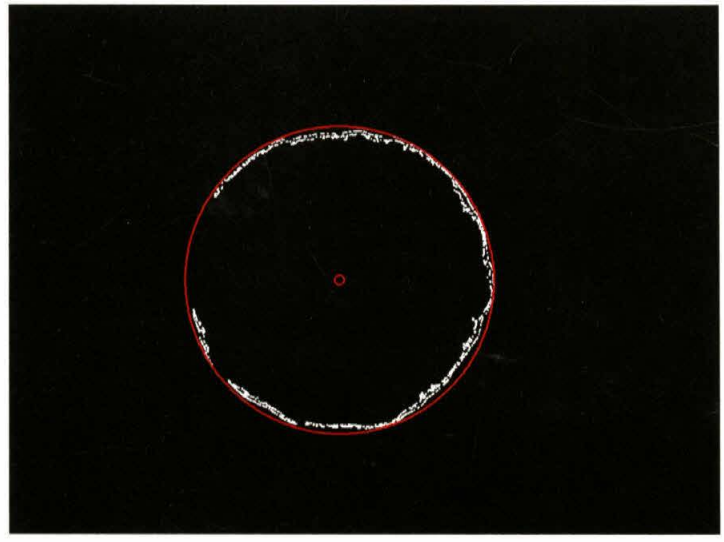

Figure 3.6: An example of a "minimum encompassing circle" (in red) drawn onto the front of which is being measured. This is a "first front" that is being measured.

number of rulers, the slope of which gives the fractal dimension.

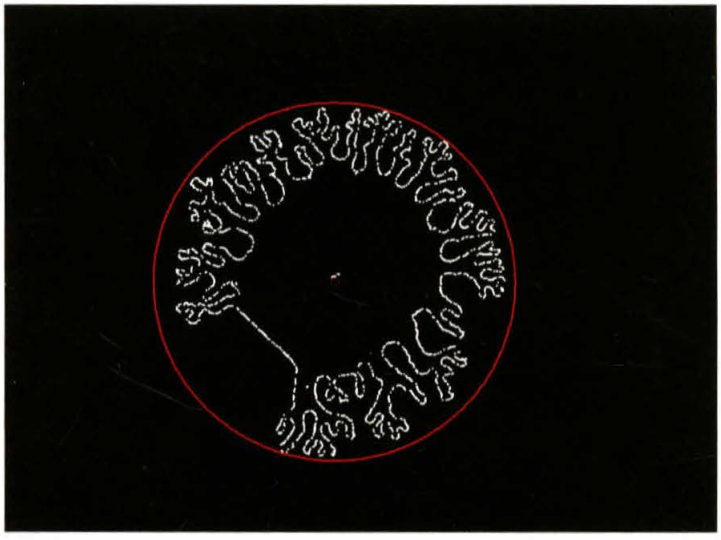

Figure 3.7: An example of a "minimum encompassing circle" (in red) drawn onto the front of which is being measured. This is an "unstable front" that is being measured.

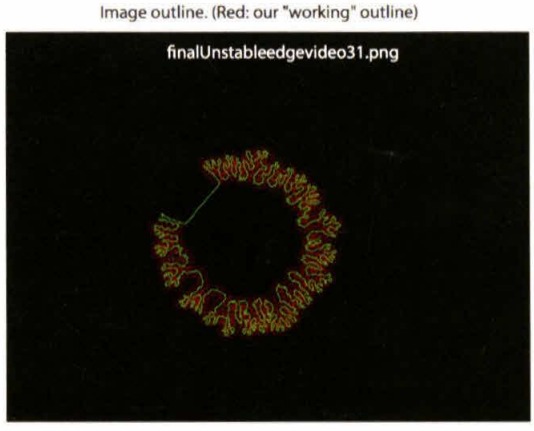

(a)

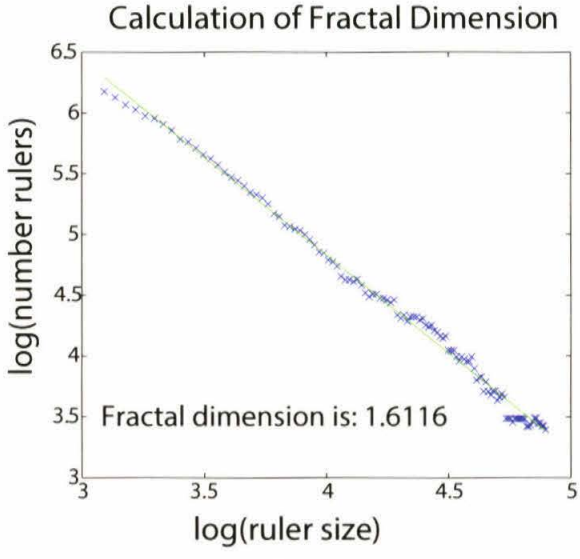

(b)

Figure 3.8: An example of the output of the program which calculates fractal dimension. In the top panel is the image, the outline in green and the "relevant" outline (with the needle cut out) in red. On the bottom panel is the log-log plot of ruler size versus number of rulers, the slope of which gives the fractal dimension, printed on the plot.

4: Data

4.1 Temperature and Humidity

The lab was always maintained at 71 °F, but humidity was harder to control since the air cycles in from the outdoors and the humidity of the outdoors changes daily (albeit the fact that we are in Pasadena, California). Hence each day has temperature and humidity data recorded. Humidity and temperature were measured using the High Performance Digital Thermo-hygrometer from Omega Engineering, Inc. As a reminder, "relative humidity" is defined as the ratio of the partial pressure of water vapor in the air to the saturated vapor pressure of water, at a specific temperature.

4.2 AOT solution surface tensions

The surface tensions of the AOT solutions I created were determined experimentally using the Pendant Drop method, as described earlier in the Experimental Setup chapter. The surface tensions are reported graphically in Figure 4.1. This plot is what we would expect of a surface tension plot, with a drop in surface tension correlated with increasing concentration, until eventually the plot flattens out. This point at which the plot flattens out is the critical micelle concentration, which we extrapolate at roughly 2.3 mM.

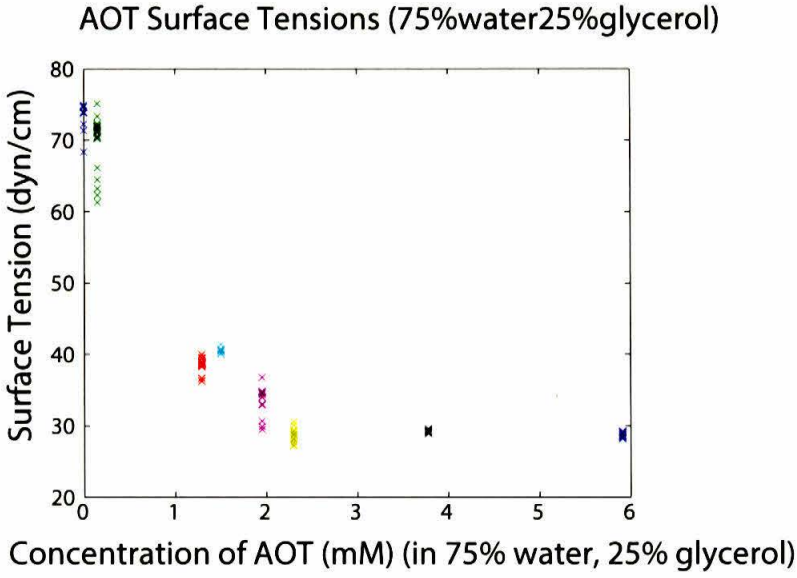

Figure 4.1: Measured values of surface tension of the prepared AOT solutions, obtained using the Pendant Drop method.

4.3 Hygroscopity of glycerol

As discussed earlier, glycerol is highly hygroscopic. As such, it seemed appropriate to take measurements of exactly how hygroscopic a thin film of glycerol is. This was done by first weighing a glass wafer alone, and then spinning the 2.5 μm film of glycerol on and immediately transferring the sample to the electronic scale. Measurements of the mass of the sample were then recorded over the course of approximately 10 minutes. The data was then reported as a fractional change in weight (defined as $\frac{\text{current weight - weight of wafer}}{\text{first measured weight - weight of wafer}}$), displayed in Figure 4.2 for a range of humidities. This plot is not terribly revealing, but it does tell us that the equilibrium weight is achieved after approximately 300 seconds. Additionally, it seems to reveal that the equilibrium weight of glycerol is higher at higher humidities than at lower humidities, which is what one would expect since there is a higher concentration of water in the air to equilibrate to.

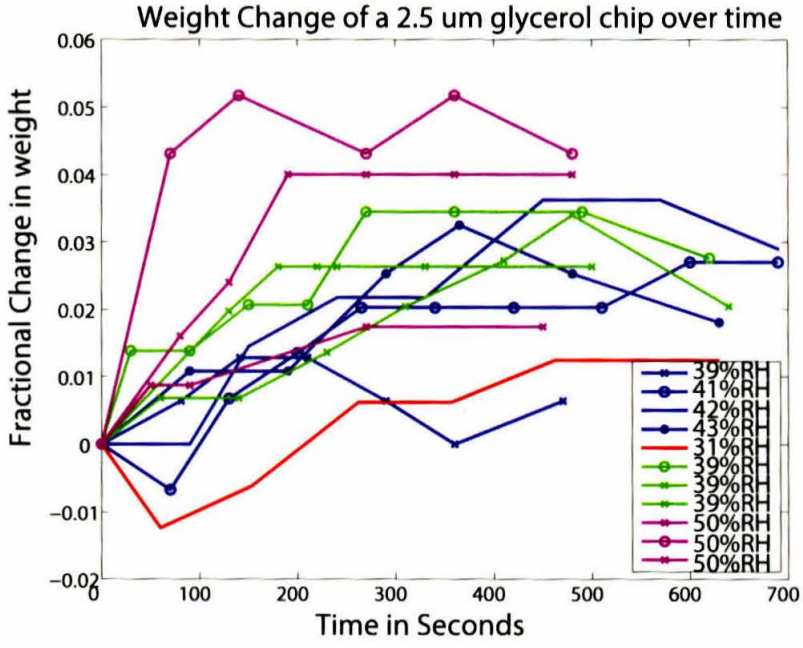

Figure 4.2: The fractional change in weight of a sample of a 2.5 μm film of glycerol, left out to sit. The fractional change is defined as the $\frac{\text{current weight - weight of wafer}}{\text{first measured weight - weight of wafer}}$. Each humidity has a separate color for visualization (Red for 31%RH, green for 39%RH, blue for roughly 40% RH, and pink for 50%RH). All samples are at roughly 71 °F.

4.4 Visual of Fingering Instability exhibited by AOT

AOT has a unique spreading pattern with fingering and bifurcating, shown in Figure 4.3 in both reflection and in transmission. We did not use reflection for the purposes of this thesis but it is nice to see what the spreading pattern looks like in reflection as it helps us gain a feel for how it casts its shadow in transmission. As we will discuss later in this chapter, AOT will not always spread like this, affected by concentration as well as humidity. However, this gives a good visual of the instabilities that AOT is capable of developing.

For reference, there are two fronts associated with the spreading– the first front that is the first to disturb the initial film, and the unstable front which breaks into undulations and fractals, which follows the first front. These fronts are visually specified in Figure 4.4. All measurements in this thesis are specified by which front is being measured.

In general we find that almost immediately after the drop is deposited, the two fronts separate, both initially stable. The first front then continues to spread, while the unstable

front breaks into very regular, densely-packed sinusoidal oscillations. This can be seen in Figure 4.5, taken approximately 0.1 seconds after deposition. Then certain undulations, relatively regularly spaced, grow faster than the others and eventually develop their own bifurcations, which in turn bifurcate. At 50% RH, up to five generations of bifurcations can have developed within one second.

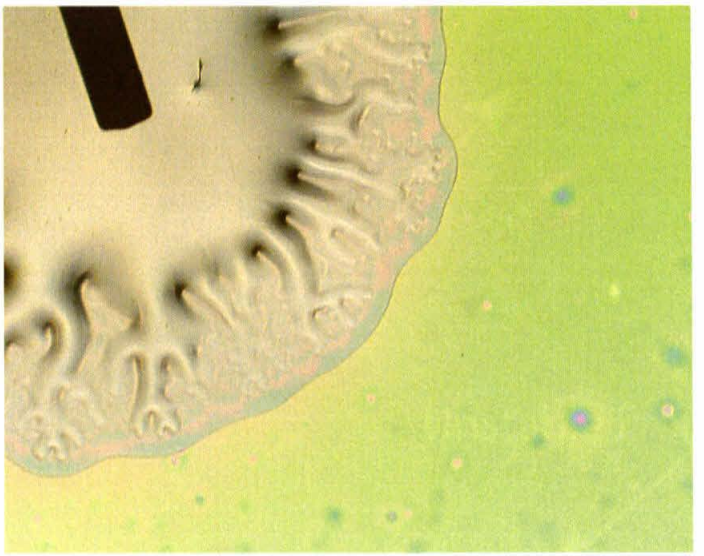

(a) AOT spreading, visualized in reflection under an optical microscope. This sample was performed on a silicon wafer.

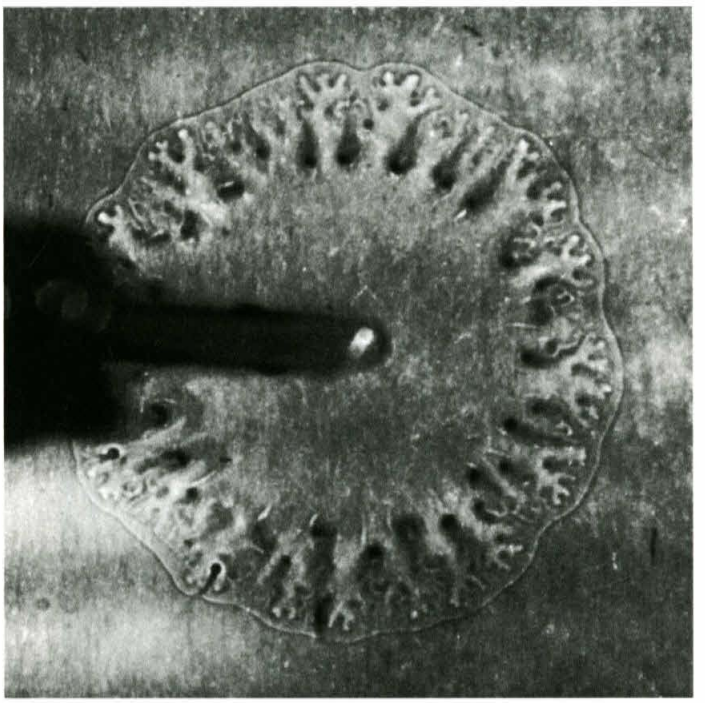

(b) AOT spreading, visualized in transmission. This sample was performed on a glass wafer.

Figure 4.3: A visual of how 1.0 μL of 1.5 mM AOT mixed in a 3:1 ratio of water:glycerol spreads on a 2.5 μm film of glycerol. The humidity is somewhere between 40-50% RH for both these images.

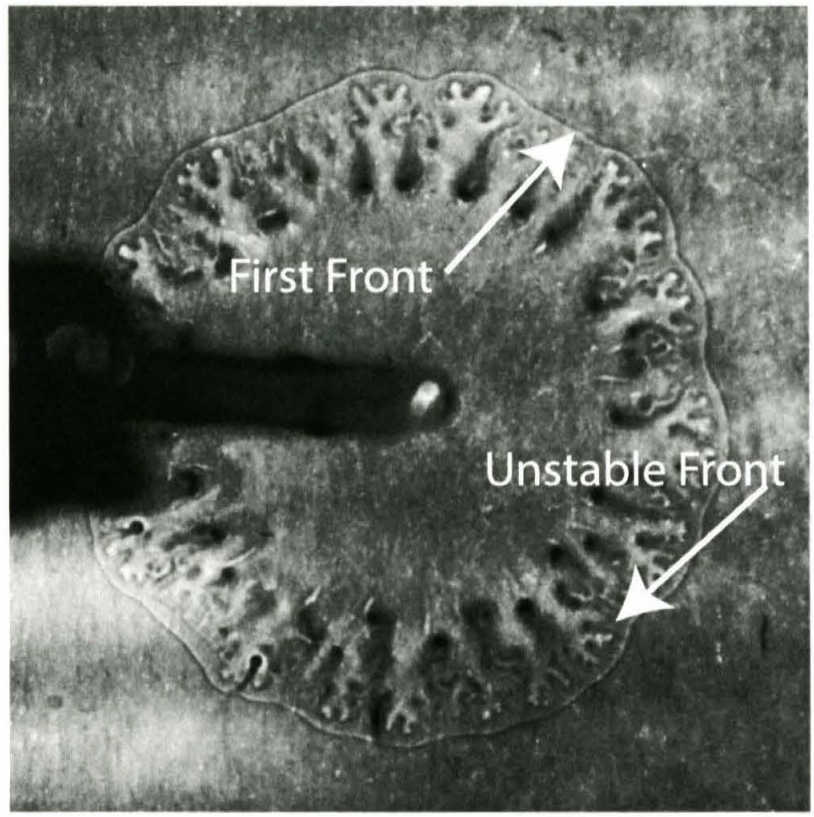

Figure 4.4: A visual specification of the fronts that are measured in this thesis. The "first front" is the first front that disturbs the initial front. The "unstable front" is behind the first front, and is the front that breaks into undulations and fractals.

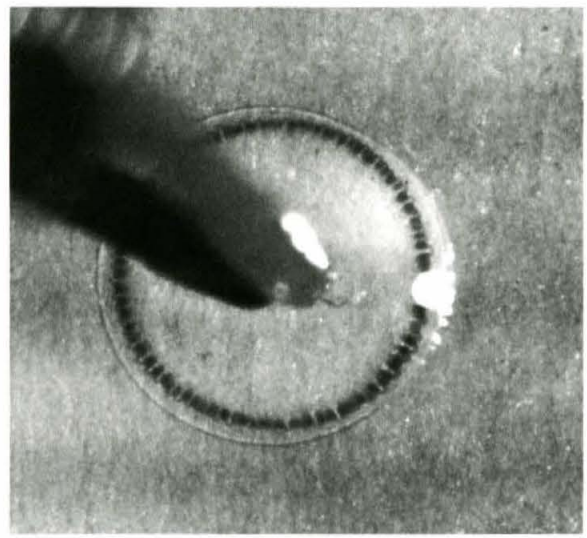

Figure 4.5: The initial instabilities exhibited by the unstable front. This image is 0.1 seconds after deposition.

4.5 Fractal Dimension

Fractal dimensions of the unstable front were calculated for some, but not all samples. Other samples have multiple fractal dimensions listed, because the fractal dimension measurement was performed on multiple images from that sample. These values are reported in Table 4.1. The overall trend seems to be that higher humidity leads to higher fractal dimensions, and that higher concentrations leads to higher fractal dimensions. All values fall between 1.45 and 1.65. Images that display fractal-like features (like in the left column of Figure 4.13) exhibit fractal dimensions closer to 1.65.

Table 4.1: An overall summary of the fractal dimensions calculated (if measured) of all chips. Fractal dimensions were not calculated for all samples. Other samples have multiple fractal dimensions listed, because the fractal dimension measurement was performed on multiple images from that sample.

Relative Humidity	1.29 mM	1.50 mM	1.95 mM	2.30 mM
25 %	1.48	1.45		
27 %	1.45	1.47		
39 %		1.58 1.56	1.51	
43 %	1.47 1.58 1.53	1.59	1.61	
51 %	1.62 1.62 1.63 1.62 1.61 1.60 1.64	1.60 1.60 1.62 1.61 1.65	1.65 1.56	

4.6 Spreading Power Laws

As has been discussed before, there are two fronts that can be measured– the first front that is the first to disturb the initial film, and the unstable front which breaks into undulations and fractals, which follows the first front. These fronts have been visually specified in Figure 4.4. All measurements in this thesis are specified by which front is being measured.

Measurements of the speeds of these fronts are performed in this thesis, but first it is appropriate to take a look at how well the data matches the reported fits. Since all the theory and previous experiments associated with this problem fit to a power-law, we attempted the same. Figure 4.6 demonstrates a fit of the data to a power law. In 4.6(a) we perform a power-law fit to the data on a linear scale, which looks pretty good and has an R-squared value of greater than 0.999. In 4.6(b) we plot the data and fit on a log-log scale, which looks very close to a line as we would hope for a power-law fit. The first value of the log-log data set has been subtracted from the rest of the values to make it suitable to be plotted on a log-log plot. As all the fits performed in this thesis look like the plots

demonstrated here, we are satisfied with the compatibility of our fits to the data.

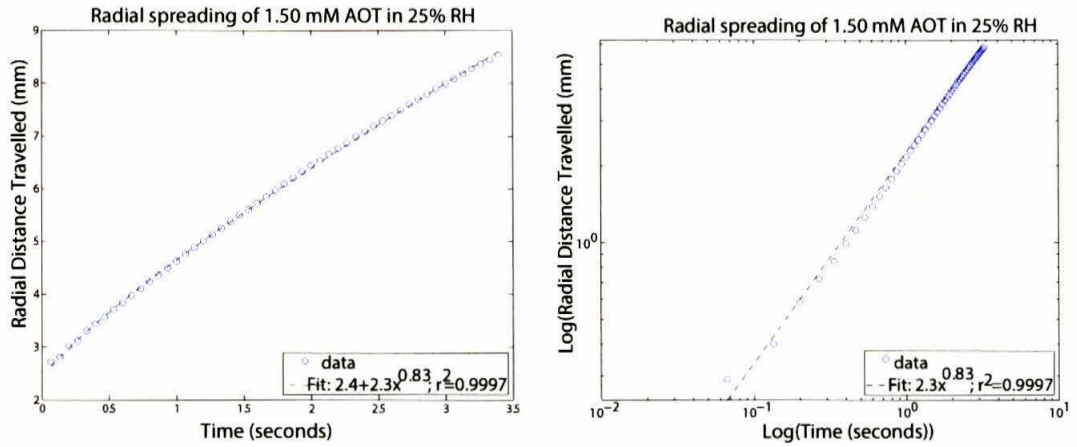

(a) Linear axes.

(b) Log-Log axes.

Figure 4.6: Example fits. All of the fits performed in this thesis fit the data as well as demonstrated in these plots.

In Table 4.2, we present a summary of the best fit power laws of the "First front" of all chips measured. In each cell, the top number is the coefficient and the bottom number is the power. As an example of how to read this data: the best fit power law of the 1.29 mM chip at 25% RH is $R = 2.4t^{0.81}$ for mm versus seconds. All chips in this table are performed at 71 °F, with 1.0 μL AOT mixed in an aqueous solution of glycerol (3:1 volume ratio of water-to-glycerol), deposited on a 2.5 μm film of glycerol upon a 51.5 mm diameter glass wafer.

There are a couple of trends to notice here. The first trend is that in samples with the same humidity, with increasing concentration (ie moving across a row) the coefficient generally grows while the power generally drops. What this means in terms of absolute velocities is that the higher concentration samples initially spread faster and then slow down, while the lower concentration samples maintain a relatively more constant speed. Another trend to notice is that at lower humidities and similar concentrations (ie moving up a column), the powers are generally higher and the coefficients lower than those at higher humidities. What this means in terms of absolute velocities is that the higher humidities samples initially spread faster and then slow down, while the lower humidity samples maintain a relatively more constant speed.

Table 4.2: An overall summary of the best fit power laws of the "First front" of all chips measured. The top number is the coefficient and the bottom number is the power. As an example of how to read this data: the best fit power law of the 1.29 mM chip at 25% RH is $R = 2.4t^{0.81}$ for mm versus seconds. All chips in this table are performed at 71 °F, with 1.0 μL AOT mixed in an aqueous solution of glycerol (3:1 volume ratio of water: glycerol), deposited on a 2.5 μm film of glycerol upon a 51.5 mm diameter glass wafer.

Relative Humidity	1.29 mM	1.50 mM	1.95 mM	2.30 mM	3.78 mM	5.91 mM	7.83 mM
25 %	2.4 0.81	2.3 0.83	2.8 0.78	3.4 0.72	3.6 0.65		
27 %	2.8 0.74	2.6 0.78	2.9 0.75	3.7 0.57	4.1 0.48		
32 %	3.1 0.81	3.0 0.78	3.5 0.72	3.9 0.70	4.5 0.49	3.9 0.41	4.0 0.36
32 %	3.1 0.84						
39 %		3.6 0.71	4.3 0.65	5.0 0.53	5.2 0.45		
43 %	3.8 0.72	3.7 0.71	5.7 0.46	5.6 0.47	4.5 0.42		
51 %	4.5 0.67	4.5 0.65	5.0 0.63	5.1 0.59			

4.7 Influence of deposited surfactant concentration

A visual of how the spreading patterns of the unstable front differ across different concentrations (everything else held fixed) can be seen in Figure 4.13, where the concentration is increased as one moves down across the images in each column. In general, for higher humidities ($>\approx 40\%$) we see multiple generations of bifurcations, which is not the case for lower humidities. At lower humidities ($<\approx 40\%$), the unstable front spreading images look more like "flower petals," with a wavy unstable edge but without multiple generations of bifurcations. One can see that increasing concentration in higher humidities (the left column) leads to more detailed and fine fingers until eventually the fingers no longer exist, and rather the unstable front is a very chaotic looking series of undulations. In lower humidities (the right column), increasing the concentration does not change the visual spreading pattern very much until a certain concentration, at which point (similar to the high humidity data) the front is a very chaotic looking series of undulations. What may be of interest is that fact that the change in these patterns occur roughly at the cmc.

Plots of how varying the concentration changes the speed of the advancing (first) front can be seen in Figures 4.8, 4.11, 4.7, 4.10, 4.12, and 4.9, which are each samples from different days (so each set of data has its own unique but constant humidity). The first value of the log-log data set has been subtracted from the rest of the values to make it suitable to be plotted on a log-log plot. The best fit power laws for these data points are also reported in Table 4.2. What one notices across these plots is that higher concentrations have a higher intercept (corresponding to a higher coefficient) and a lower slope (corresponding to a lower power). Each data set looks roughly linear on a log-log scale, corresponding to a power law.

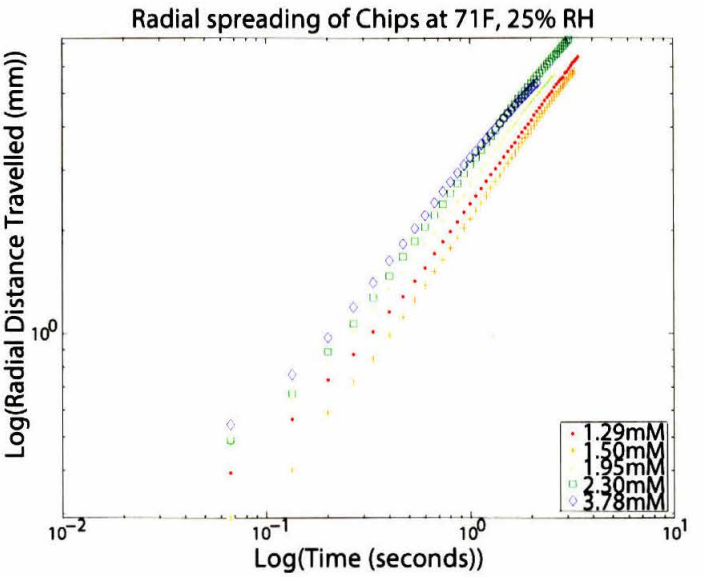

Figure 4.7: A comparison of how only increasing concentration affects the spreading rates of the first front. All this data is 1.0 μL AOT mixed in an aqueous solution of glycerol (3:1 volume ratio of water: glycerol), deposited on a 2.5 μm film of glycerol upon a 51.5 mm diameter glass wafer. Temperature was 71 °F, at 25% relative humidity.

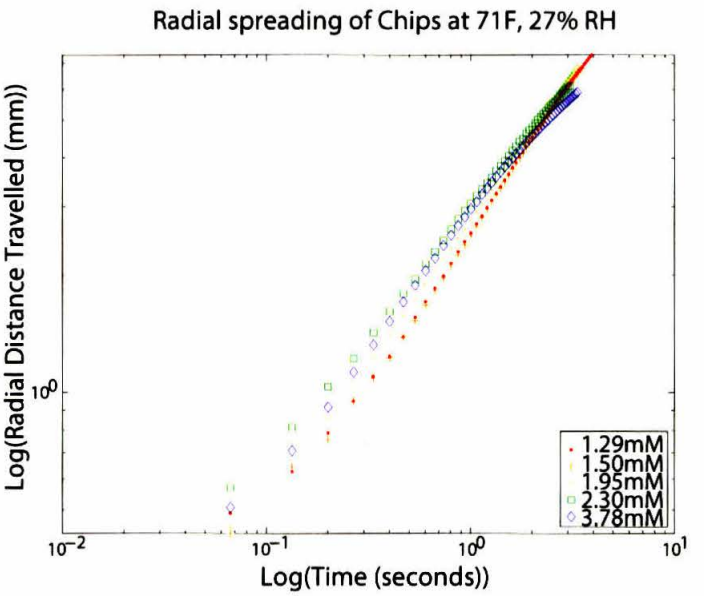

Figure 4.8: A comparison of how only increasing concentration affects the spreading rates of the first front. All this data is 1.0 μL AOT mixed in an aqueous solution of glycerol (3:1 volume ratio of water: glycerol), deposited on a 2.5 μm film of glycerol upon a 51.5 mm diameter glass wafer. Temperature was 71 °F, at 27 % relative humidity.

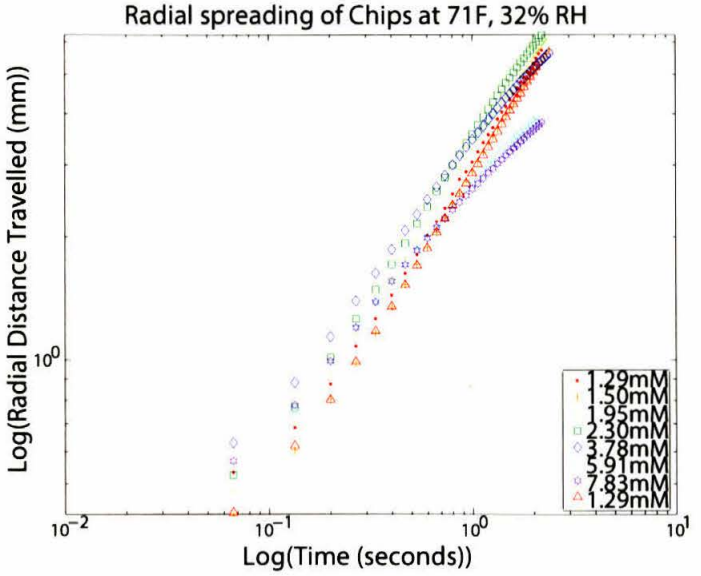

Figure 4.9: A comparison of how only increasing concentration affects the spreading rates of the first front. All this data is 1.0 μL AOT mixed in an aqueous solution of glycerol (3:1 volume ratio of water: glycerol), deposited on a 2.5 μm film of glycerol upon a 51.5 mm diameter glass wafer. Temperature was 71 °F, at 32% relative humidity.

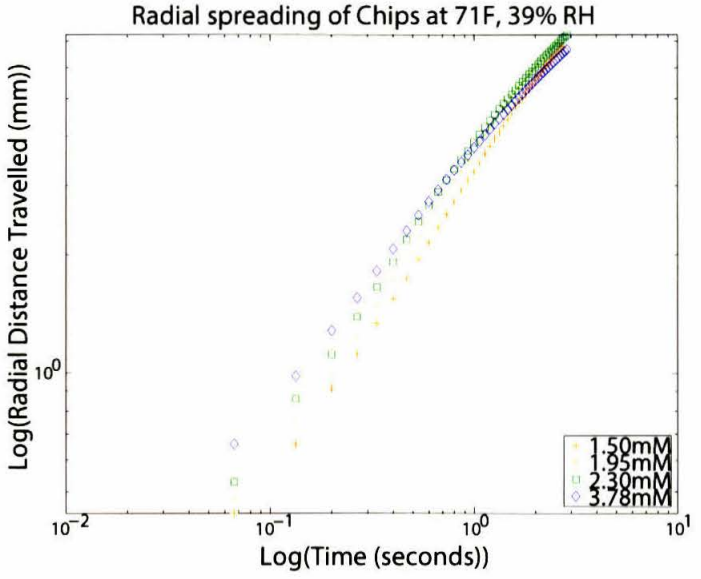

Figure 4.10: A comparison of how only increasing concentration affects the spreading rates of the first front. All this data is 1.0 μL AOT mixed in an aqueous solution of glycerol (3:1 volume ratio of water: glycerol), deposited on a 2.5 μm film of glycerol upon a 51.5 mm diameter glass wafer. Temperature was 71 °F, at 39% relative humidity.

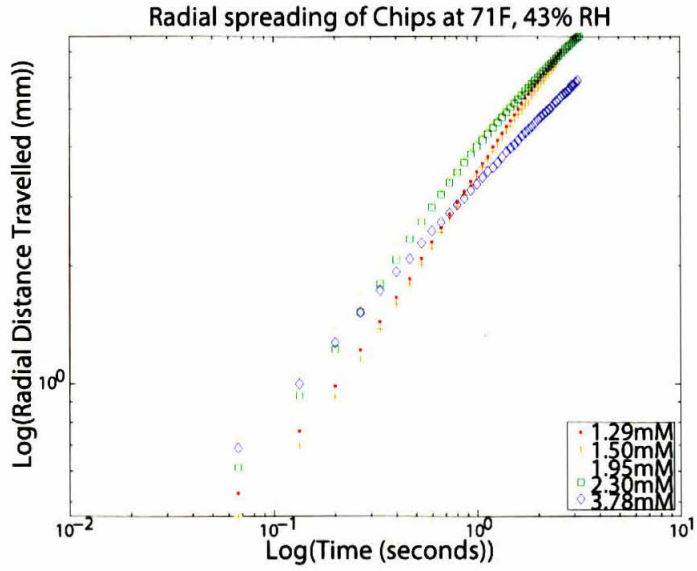

Figure 4.11: A comparison of how only increasing concentration affects the spreading rates of the first front. All this data is 1.0 μL AOT mixed in an aqueous solution of glycerol (3:1 volume ratio of water: glycerol), deposited on a 2.5 μm film of glycerol upon a 51.5 mm diameter glass wafer. Temperature was 71 °F, at 43% relative humidity.

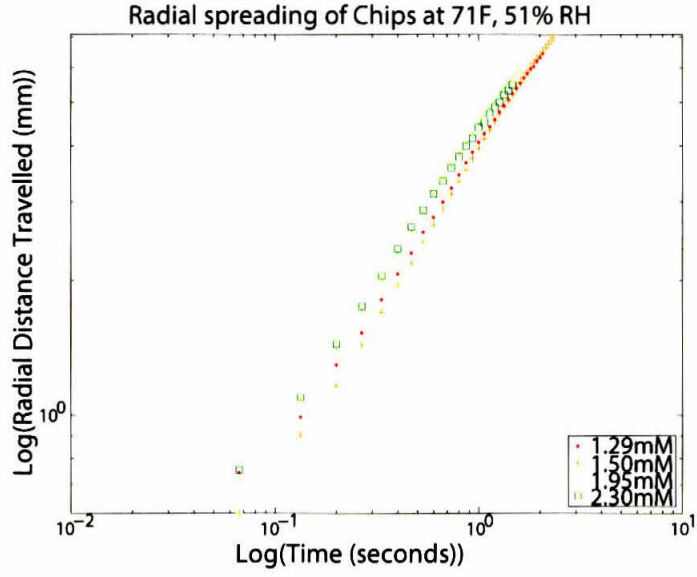

Figure 4.12: A comparison of how only increasing concentration affects the spreading rates of the first front. All this data is 1.0 μL AOT mixed in an aqueous solution of glycerol (3:1 volume ratio of water: glycerol), deposited on a 2.5 μm film of glycerol upon a 51.5 mm diameter glass wafer. Temperature was 71 °F, at 51% relative humidity.

4.8 Influence of ambient relative humidity

Unfortunately, very near the end of my senior year, I discovered that the ambient humidity of the atmosphere was drastically changing the spreading patterns of my samples. Figure 4.13 gives a visual on this, comparing side-by-side the exact same experimental-parameter samples on days of differing humidity. As one can see, the samples on more humid days exhibit more ramified fingering in the unstable front with multiple generations of bifurcations. The samples on less humid days do not exhibit multiple generations of bifurcations, although they do show the same initial instability in the unstable front which only ends up growing and not bifurcating, producing a spreading image which looks more like "flower petals."

Plots of how varying the humidity changes the speed of the advancing (first) front can be seen in Figures 4.14, 4.15, 4.16, 4.17, and 4.18, each of which are samples of the same concentration (as well as volume, film thickness. etc), with the only differing factor within each plot being the humidity at which these experiments were conducted. These data points are plotted on a log-log scale. The first value of the log-log data set has been subtracted from the rest of the values to make it suitable to be plotted on a log-log plot. The best fit power laws for these data points are also reported in Table 4.2. As one can see for each plot (and hence each concentration), the data points for each humidity are more or less parallel with higher humidities showing a slightly smaller slope (corresponding to roughly equal powers and a slight increase in power for higher humidities). Additionally, the higher humidities in each data set have a higher intercept than the lower humidity data, corresponding to a higher coefficient in the power law fits for higher humidities. Again, each data set is roughly linear on the log-log scale, meaning a power-law fit is well-suited here.

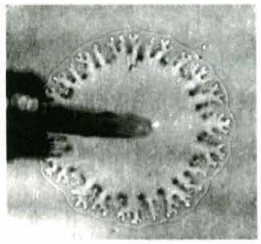

(a) 1.29mM, 48%RH.

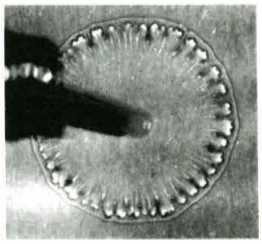

(b) 1.29mM, 25%RH.

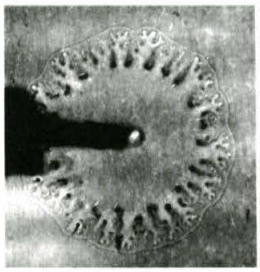

(c) 1.50mM, 48%RH.

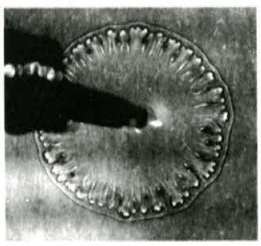

(d) 1.95mM, 25%RH.

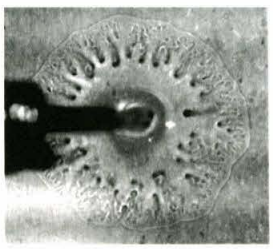

(e) 1.95mM, 48%RH.

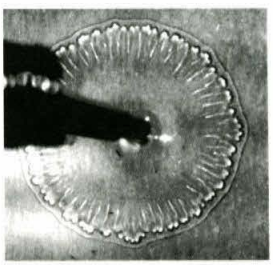

(f) 1.95mM, 25% RH.

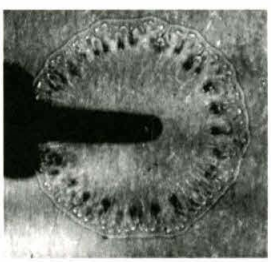

(g) 2.30mM, 48% RH.

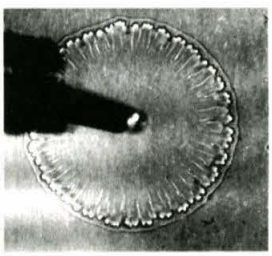

(h) 2.30mM, 25% RH.

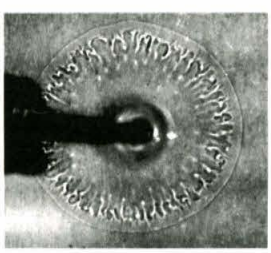

(i) 3.78mM, 48% RH.

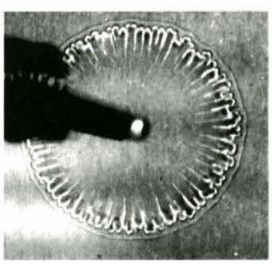

(j) 3.78mM, 25% RH.

Figure 4.13: The effect of varying concentrations of AOT and varying humidities on spreading patterns. All other factors are held fixed. These are 1.0 μL of the specified concentration of AOT in an aqueous solution of glycerol (3:1 ratio of water to glycerol), deposited on a 2.5 μm film of glycerol, at 71 °F.

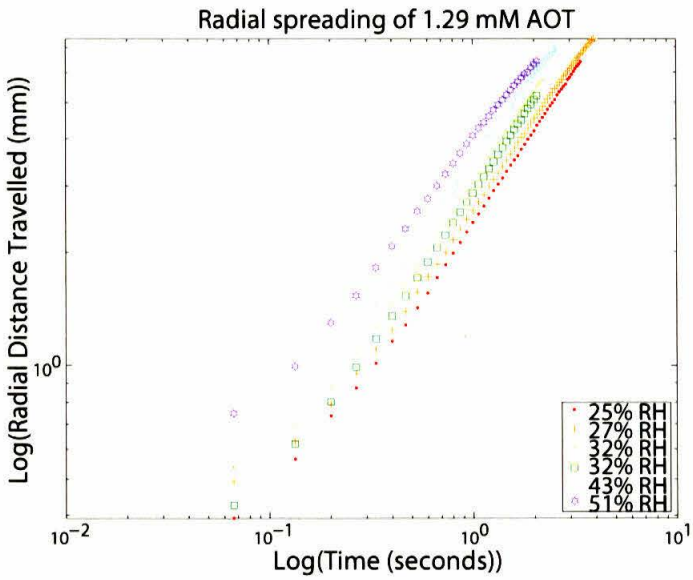

Figure 4.14: A comparison of how only changing the humidity affects the spreading rates of the first front. All this data is 1.0 μL 1.29 mM AOT mixed in an aqueous solution of glycerol (3:1 volume ratio of water: glycerol), deposited on a 2.5 μm film of glycerol upon a 51.5 mm diameter glass wafer. Temperature was 71 °F.

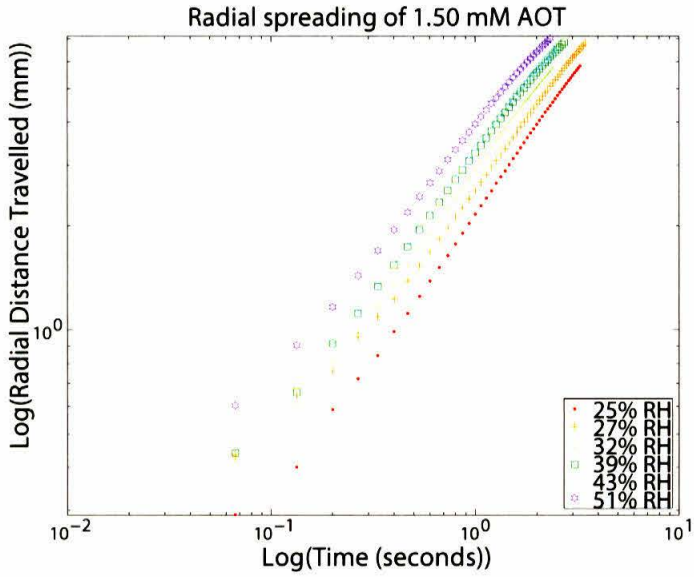

Figure 4.15: A comparison of how only changing the humidity affects the spreading rates of the first front. All this data is 1.0 μL 1.50 mM AOT mixed in an aqueous solution of glycerol (3:1 volume ratio of water: glycerol), deposited on a 2.5 μm film of glycerol upon a 51.5 mm diameter glass wafer. Temperature was 71 °F.

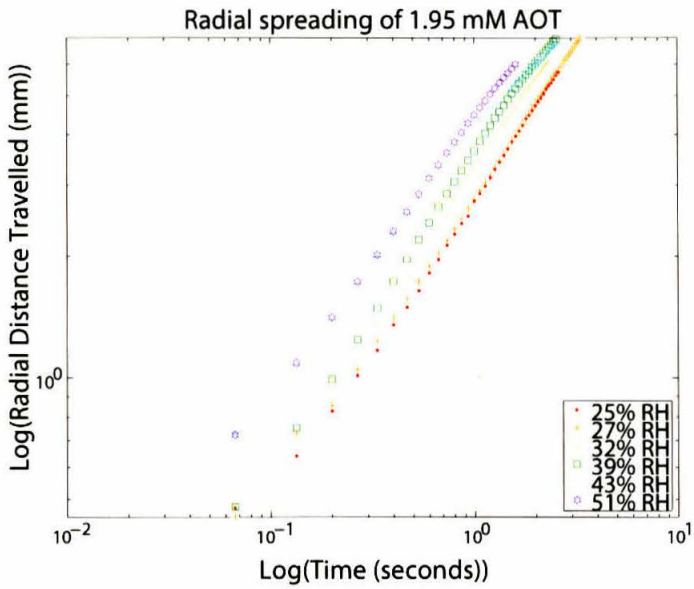

Figure 4.16: A comparison of how only changing the humidity affects the spreading rates of the first front. All this data is 1.0 μL 1.95 mM AOT mixed in an aqueous solution of glycerol (3:1 volume ratio of water: glycerol), deposited on a 2.5 μm film of glycerol upon a 51.5 mm diameter glass wafer. Temperature was 71 °F.

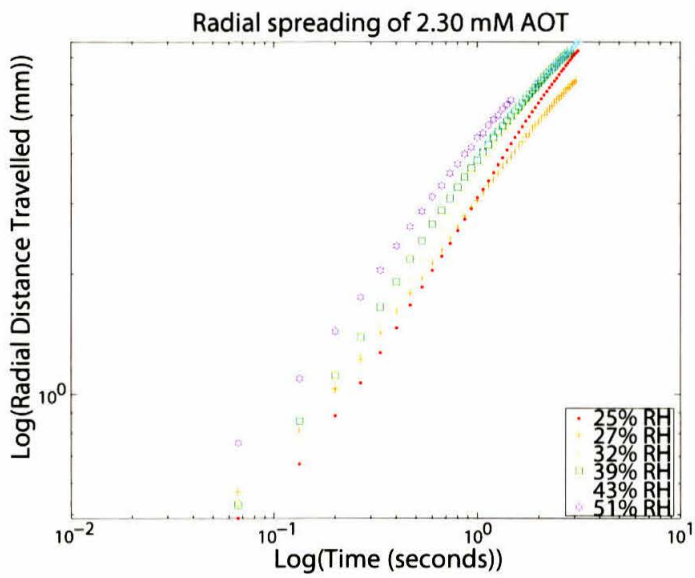

Figure 4.17: A comparison of how only changing the humidity affects the spreading rates of the first front. All this data is 1.0 μL 2.30 mM AOT mixed in an aqueous solution of glycerol (3:1 volume ratio of water: glycerol), deposited on a 2.5 μm film of glycerol upon a 51.5 mm diameter glass wafer. Temperature was 71 °F.

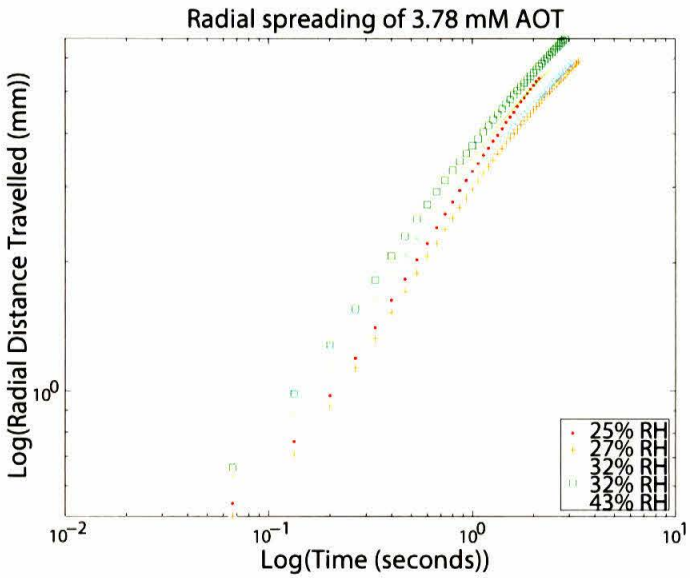

Figure 4.18: A comparison of how only changing the humidity affects the spreading rates of the first front. All this data is 1.0 μL 3.78 mM AOT mixed in an aqueous solution of glycerol (3:1 volume ratio of water: glycerol), deposited on a 2.5 μm film of glycerol upon a 51.5 mm diameter glass wafer. Temperature was 71 °F.

4.9 Influence of initial deposited droplet volume

This analysis of the effect of volume on the spreading is not thorough and the data in this section cannot be compared to the rest of the data in this thesis because this data has no atmospheric humidity data associated with it. Additionally, the syringe and chip used in this section are different from those used in the rest of this thesis. In any case, the samples in this section were all conducted on the same day, so in itself it provides some insight on the effect of volume on the spreading since humidity is relatively constant within any given day.

Wafers used in this section were 2.54cm x 2.54cm in width and length and 0.93 to 1.05 mm in thickness, cut from Gold Seal MicroSlides. The syringe was a Hamilton Gastight 10 μL Syringe of the 1701 Series. The needle was a 22s gauge, point-style 3 (blunt point) needle, 2" in length. Table 4.3 reports the best fit power law parameters for both the unstable fingering front as well as the first front for the samples in this volume-varying study. The first listed set of values is for the "first front," in italics. The second listed set of values is for the "unstable front," in normal font.

More or less, it appears that the volume does not affect the power law spreading of the unstable front (in normal font) drastically, although one could argue that at the largest volume of 2.5 μL, the power is noticeably higher than those of the smaller volumes. The first fronts (in italics) have a more noticeable pattern of a higher power and arguably lower coefficient with larger volumes. If one tries to compare the power laws between the two fronts, one can see that at 1.5 μL, the first front generally has a slightly lower power than the unstable front, although it does still spread faster because of the coefficient. At 2.0 μL and 2.5 μL, the power is always higher and the coefficient lower in the first front than in the unstable front.

Figure 4.19 plots all of the volume-varying sample's first front spreading data on the same plot for visualization. Overall, it appears that larger volumes spread faster.

Figure 4.20 plots all of the volume-varying sample's unstable front spreading data

Table 4.3: Coefficient followed by power of the best fit power laws on the volume-varying samples. The first listed set of values is for the "first front," in italics. The second listed set of values is for the "unstable front," in normal font. As an example of how to read this data: the best fit power law of the unstable front of Sample 1 at 1.5 μL is $R = 5.1t^{0.49}$ in mm versus seconds. All chips in this table are performed at 71 °F with the specified volume of AOT mixed in an aqueous solution of glycerol (3:1 volume ratio of water: glycerol), deposited on a 2.5 μm film of glycerol upon a 2.54cm x 2.54cm glass slide. Although the humidity data here is not quantitatively known, it is known that the humidity for all these samples is the similar because they were all conducted on the same day.

Volume AOT deposited	Sample 1	Sample 2	Sample 3	Sample 4
1.5 μL	*5.7; 0.46* 5.1; 0.49	*5.7; 0.45* 5.7; 0.46	*6.1; 0.40* 5.7; 0.42	
2.0 μL	*4.0; 0.72* 6.5; 0.42	*3.9; 0.63* 4.5; 0.57	*4.4; 0.62* 6.1; 0.44	*4.0; 0.56* 5.46; 0.44
2.5 μL	*4.2; 0.74* 5.4; 0.62	*4.3; 0.72* 5.5; 0.61	*4.0; 0.85* 5.2; 0.68	

on the same plot for visualization. Overall, it appears that larger volumes spread faster, although it is not as obvious as the trend seen in the first front.

Figure 4.21 plots all of the volume-varying study sample's fractal dimension data for the unstable front on the same plot for visualization. The fractal dimension grows for the first fractions of a second, the time during which the instabilities first start to appear and develop. At approximately 0.6 seconds, the patterns have hit their final fractal dimension and maintain that value. At this point, the fractals are still bifurcating and creating new generations, but they are self-repetitive so the fractal dimension remains constant. The average fractal dimension (calculated from 0.7 seconds onwards) is 1.57 for the 1.5 μL samples, 1.59 for the 2.0 μL samples, 1.60 for the 2.5 μL samples, and 1.59 overall.

Although the humidity data for these samples is not known, we estimate it in the range of 40%-50% RH because its spreading patterns are similar to those exhibited in the samples we know to be in that range.

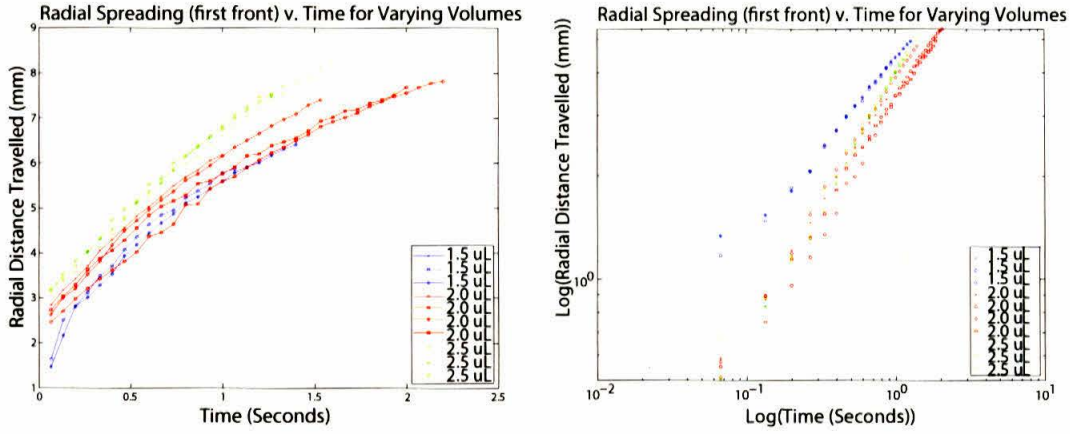

(a) Linear axes. (b) Log-Log axes.

Figure 4.19: The effect of varying volumes on the first front spreading rates, plotted both linearly and on a log-log plot. All the 1.5 μL samples are plotted in blue, the 1.5 μL samples in red, and the 2.5 μL samples in green. All chips are performed at 71 °F with the specified volume of AOT mixed in an aqueous solution of glycerol (3:1 volume ratio of water: glycerol), deposited on a 2.5 μm film of glycerol upon a 2.54cm x 2.54cm glass slide. Although the humidity data here is not quantitatively known, it is known that the humidity for all theses samples is the same because they were all conducted on the same day.

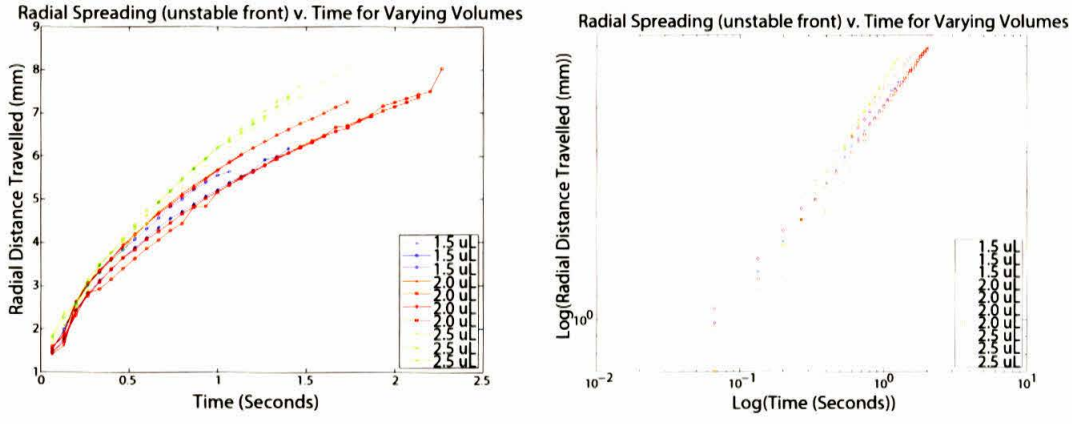

(a) Linear axes. (b) Log-Log axes.

Figure 4.20: The effect of varying volumes on the unstable front spreading rates, plotted both linearly and on a log-log plot. All the 1.5 μL samples are plotted in blue, the 1.5 μL samples in red, and the 2.5 μL samples in green. All chips are performed at 71 °F with the specified volume of AOT mixed in an aqueous solution of glycerol (3:1 volume ratio of water: glycerol), deposited on a 2.5 μm film of glycerol upon a 2.54cm x 2.54cm glass slide. Although the humidity data here is not quantitatively known, it is known that the humidity for all theses samples is the same because they were all conducted on the same day.

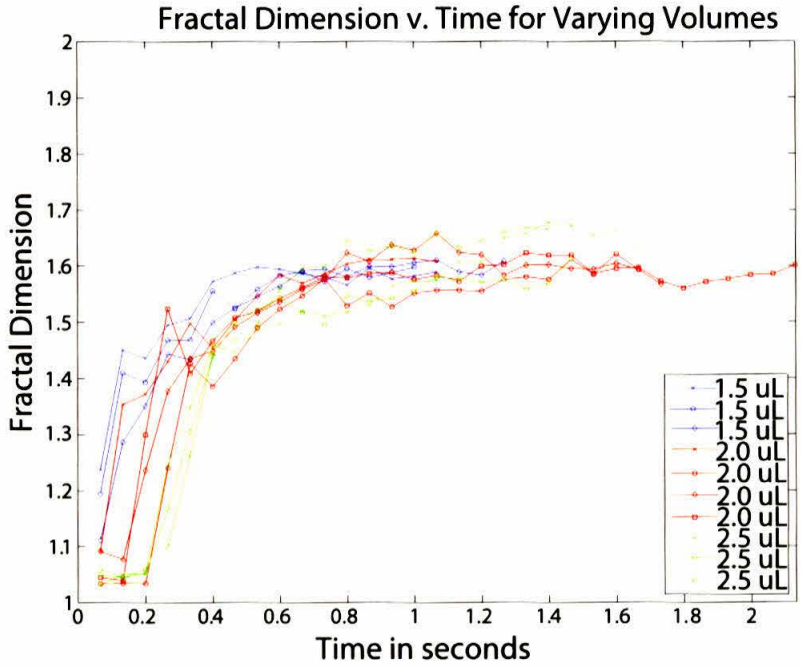

Figure 4.21: How the fractal dimension of different volume samples varies with time. All the 1.5 μL samples are plotted in blue, the 1.5 μL samples in red, and the 2.5 μL samples in green.

4.10 Error Analysis

All fit parameters in this thesis are reported to two significant figures because our least accurate measurement was the pixel-to-millimeter conversion. In this conversion, we converted distances on our camera images (in pixels) to numbers meaningful to humans (millimeters). This conversion involved a pixel value of two significant figures to be converted to 1 millimeter. Hence, all subsequent fits are reported at two significant figures.

A further uncertainty analysis is presented. The following measurements were devoted solely to determining the uncertainty in samples conducted on a day with everything held constant: humidity, volume, concentration, etc. The data for the best-fit power law for the spreading first front is presented in Table 4.4.

Table 4.4: An error analysis by analyzing the the power laws for three samples done on the same day. All this data is 1.0 μL 1.29 mM AOT mixed in an aqueous solution of glycerol (3:1 volume ratio of water: glycerol), deposited on a 2.5 μm film of glycerol upon a 51.5 mm diameter glass wafer. Temperature was 71 °F, 37 % Relative Humidity.

Sample 1	Sample 2	Sample 3
4.1; 0.66	3.6; 0.71	3.9; 0.70

This demonstrates the uncertainty associated with any given measurement. The uncertainty associated with these measurements are 3.9 ± 0.1 on the coefficient and 0.69 ± 0.02 on the power. I suspect that most of the variation in measurements here arises from the amount of time it takes to transfer the sample from the spincoater to the imaging station. If we look back at Figure 4.2 for hygroscopic data, we see that the equilibrium for the glycerol-water film is hit near 300 seconds. However, the time scale of the experiment takes anywhere between 40 to 60 seconds. Hence, in this time period, the water content of the glycerol film is still changing. One might argue that this problem could be avoided by waiting until the equilibrium is reached. This is non-ideal because the glycerol experiences dewetting on the chip, which becomes extremely obvious past 90 seconds. We aim to conduct the experiment as quickly after spincoating as possible, which becomes physically possible approximately 50 seconds after spincoating. This inevitably leads to inconsistencies in our measurements, as we can see. We must also remember, however,

that measurements are always prone to variations, and what I have discussed is merely an observation that may be enhancing the errors we see. Ultimately, this is only one of the many potential causes of variation in our measurements.

4.11 Chapter Summary

As a summary of what I covered in this chapter:

a) I reported the surface tensions of various AOT concentrations dissolved in an aqueous solution of glycerol (3:1 ratio of water to glycerol by volume) and report the cmc to be approximately 2.3 mM.

b) I performed an investigation of the hygroscopity of a 2.5 μm film of glycerol and found that the equilibrium compositions of the film are reached at approximately 300 seconds after removal from the spincoater.

c) I show that power laws are indeed a suitable fit to the radial spreading data for both the first front and the unstable front. Additionally, the parameters of the power law fit are affected by both concentration and humidity. An increase in concentration across constant humidity leads to higher coefficients and lower powers. An increase in humidity across constant concentration also leads to higher coefficients and lower powers.

d) The purely visual aspect of spreading patterns are drastically different in varying humidities. The spreading of samples in higher humidities leads to more generations of bifurcations, and hence a more fractal-like pattern.

e) Varying the volume of surfactant deposited does not change the fractal dimension of the spreading pattern. Higher volumes do, however, lead to slightly higher powers and lower coefficients in the power-law fits of radial spreading.

f) We report fractal dimensions of AOT spreading on glycerol to be between 1.45 and 1.65. The "true" fractal dimensions in which multiple generations of bifurcations happen, have a fractal dimension of approximately 1.65.

5: Analysis

5.1 Spreading Rates

Spreading rates are predicted by theory to follow a power law. This I have confirmed through my experiments for both the first and unstable front. However, theory also predicts the power law to follow r^4 or $r^2 \sim \frac{MH_0(\sigma_{film}-\sigma_{surfactant})}{\mu}t$, where M is the surfactant mass, H_0 is initial film thickness, σ is surface tension, and μ is the film viscosity. In either case, the theory therefore predicts a change in *coefficient* with increasing concentration, since concentration is related to surface tension, represented in the coefficient through either a square root or through a fourth root. The general relation of increasing coefficient with increasing concentration we can confirm with our data. The theory also predicts a constant *power* across increasing concentrations. This statement is refuted by our data. I will discuss these in more detail as follows.

In terms of the coefficient, we do find (as theory suggests) that the coefficient of the power law increases with increasing concentration of surfactant. Since the surface tension of the film remains the same, we expect the value $\sigma_{film} - \sigma_{surfactant}$ in the coefficient to increase with increasing concentration of surfactant. This is because an increase in concentration of surfactant means a decrease in the surface tension of the surfactant, which leads to a bigger difference in $\sigma_{film} - \sigma_{surfactant}$. Hence, this part of the theory is supported. Additionally, we would expect the difference $\sigma_{film} - \sigma_{surfactant}$ to remain constant beyond the cmc of the surfactant, since the definition of the cmc is that the surface tension of the solution does not change beyond the cmc. If we look at the limited data we have of power-law fits beyond the cmc (which we predicted around 2.3 mM), we see that the coefficients remain roughly constant past the cmc. Hence, the theory regarding the coefficients of the power law is not refuted by our data.

In terms of the power, our data does not agree with the theory. The theory does not allow for any factors in our setup to affect the power in the power law spreading. How-

ever, our data shows that the power drops with increasing concentration, in conflict with the theory. Hence, the theory needs adjustment. Jensen and Grotberg [20] suggest that the power of the spreading front in axisymmetric geometry varies as $a = \frac{1}{4}(1+\alpha)$, and that the power of the local surfactant concentration varies as $b = \frac{1}{2}(1-\alpha)$, where the total mass of the surfactant may be expressed as $M \sim t^{\alpha}$ where t is time. Thus a strip or a drop of surfactant is represented by $\alpha = 0$, and a front by some $\alpha > 0$. Generally, we assume that $\alpha = 0$ because we deposit a finite amount of surfactant on the film, in which case the power of the spreading front must be $\frac{1}{4}$. But perhaps if we take the value α to be nonzero, we may be able to explain the changing power of the spreading front as concentration varies. After all, Jensen and Grotberg did suggest that the power of the spreading front, a, and the power of the local surfactant concentration, b, are related to each other. Perhaps even taking α to be nonzero is appropriate because our droplet in comparison to our film thickness is quite large, making the droplet seem more like an infinite source of surfactant rather than a droplet. Hence, pursuing what Jensen and Grotberg suspected may be the correct path to discover the dynamics of this system.

5.2 The Effects of Humidity on Spreading Rates

The fact that humidity affects the spreading patterns is something of interest to analyze. Humidity affecting the spreading can come into play either through film viscosity or through film surface tension, as the glycerol film absorbs water. We know that the surface tension of water (73 dyn/cm) and glycerol (64 dyn/cm) are fairly close, and that the water makes up a fairly small percentage of the new film. Specifically, looking back at Figure 2.4, we can see that in the relevant humidity range of 20-50%, the equilibrium percent glycerol by weight is approximately 80-95%. Gallant [13] performed a study on the surface tensions of aqueous glycerol, and the results are shown in Figure 5.1. As we can see, the surface tensions of the compositions of aqueous glycerol relevant to our studies do not vary by more than 5 dyn/cm, and is therefore not significant enough to affect our results to the extent we see. Hence, we can somewhat disregard the surface tension effects of the hygroscopically absorbed water affecting the spreading patterns.

The other factor to consider is the viscosity of the aqueous glycerol. The viscosity of water (1 mPa·s) and glycerol (1.4 Pa·s) differ by greater than three orders of magnitude. Sheely [43] performed a study on the viscosities of aqueous glycerol, and the results pertinent to this study are summarized in Figure 5.2. As we can see, the viscosity of aqueous glycerol changes drastically between 80-95% glycerol, by almost a factor of 5.

Let's take a quantitative look at our values versus theory. We can pull two data points, each at 1.29 mM concentration, but one from 25% RH and one from 51% RH. If we look at Figure 2.4 again, we see that the equilibrium concentration at 25% RH is approximately 95% glycerol by weight, and the equilibrium concentration at 50% RH is approximately 83% glycerol by weight. Assuming the glycerol films are able to reach equilibrium by the time of the experiment (which is, of course, a generous assumption), we can next look at Figure 5.2 and find that the absolute viscosity of the films should be approximately 500 centipoises for the 25% RH sample, and 100 centipoises for the 51% RH sample. This is a factor of 5 difference between the two samples.

Theory predicts a spreading law of either r^4 or $r^2 \sim \frac{MH_0(\sigma_{film}-\sigma_{surfactant})}{\mu}t$, where M is the surfactant mass, H_0 is initial film thickness, σ is surface tension, and μ is the film viscosity. Viscosity therefore comes into play as either an inverse square or an inverse fourth root in relation to the spreading law coefficient. If we assume that the $r \sim t^{1/4}$ theory is correct, we should get approximately $(\frac{500}{100})^{1/4} = 1.5$ as the ratio of the coefficients in front for our two data points. If we assume that the $r \sim t^{1/2}$ theory is correct, we should get approximately $(\frac{500}{100})^{1/2} = 2.2$ as the ratio of the coefficients in front. This is, of course, flawed because we already know that the power law is neither of those values, but rather somewhere in the range 0.6 - 0.8, since these are the values of the fits of the two samples. So let's instead say that the power is 0.7, in which case the ratio of the coefficients would be $(\frac{500}{100})^{0.7} = 3.1$. The real ratio of the two coefficients, based on the power law fits, is $\frac{4.474}{2.420} = 1.85$. This value is between the two theory values. This is of course non-conclusive, but it paves some directionality for future studies of the theory in how viscosity affects thin film spreading of surfactants.

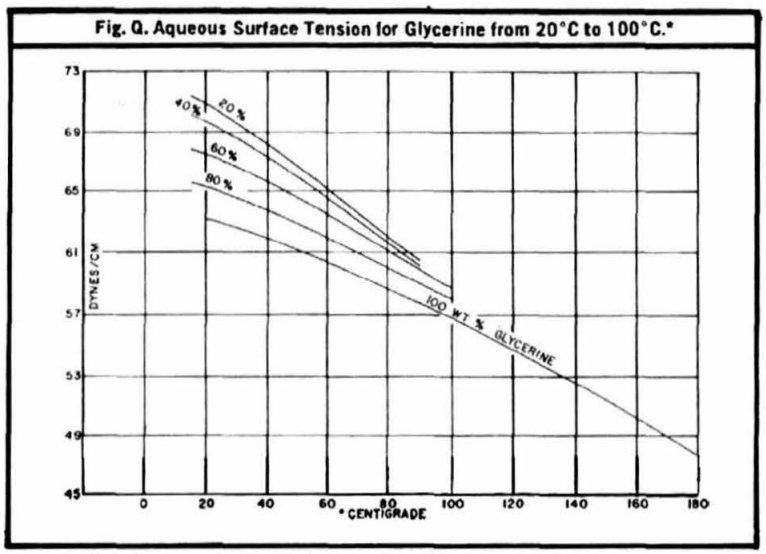

Figure 5.1: Surface tension measurements for aqueous glycerol, courtesy of [13].

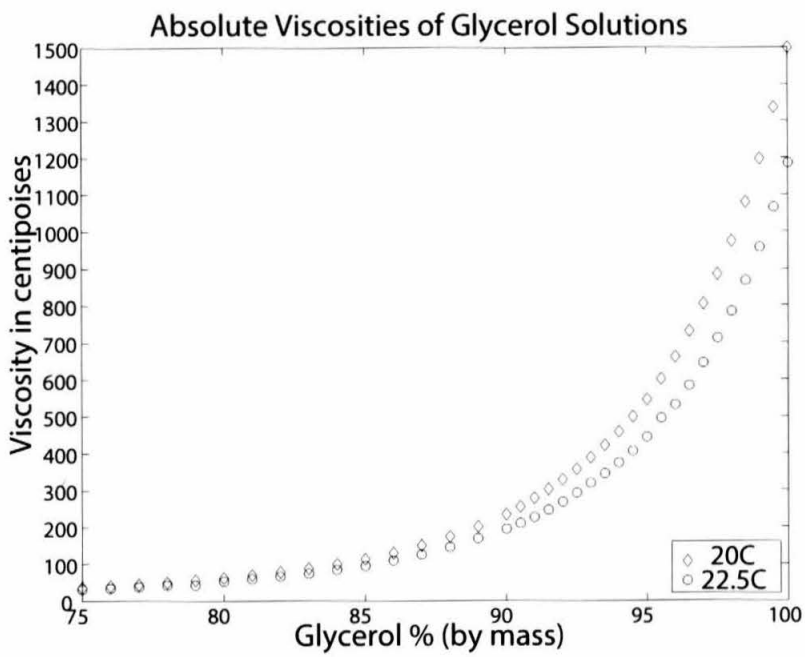

Figure 5.2: Absolute viscosity measurements of aqueous glycerol, courtesy of [43].

5.3 Fractal Dimension

First a disclaimer: fractal dimensions are neither a very precise nor accurate number, and fractal dimensions are not a unique descriptor. In any case, the values we report for the fractal dimensions of the unstable front of AOT spreading on glycerol range between 1.45 to 1.65. The images that we consider more of "true fractals," ie exhibiting multiple generations of fingering, have fractal dimensions of approximately 1.65. It may be of interest to note that the reported values of fractal dimension for viscous fingering in a Hele-Shaw are reported at 1.7 [33], similar to the values we report. This is of interest because it may indicate similar processes at work between our experiment and the Hele-Shaw experiment, although we can already rule out diffusion driven aggregation and viscous fingering because these are not pertinent to Marangoni flow.

Additionally, it is of interest to note that only at relatively high humidities ($>\approx$ 40%RH) are multiple generations of bifurcations exhibited in the unstable front of AOT spreading. At lower humidities ($<\approx$ 40%RH), the instability is present in the unstable front, but the instabilities do not bifurcate, resulting in a more "flower-like" pattern with a wavy edge but no self-similarity on multiple scales. If our assumption is correct that humidity affects the spreading patterns through changing the film viscosity, then film viscosity will also have a say in the kinds of instabilities and patterns that develop in the unstable front. Perhaps the intuitive way to think about this is through laminar versus turbulent flows. When a system possesses high viscosity, it is characterized as laminar flow which has less drag and is described more as "smooth." When a system possesses low viscosity on the other hand, it is characterized as turbulent flow which has more drag and is characterized by chaos which is described as "rough."

6: Conclusions and Future Work

6.1 Conclusions

We have shown that in our setup of AOT spreading on a 2.5 micron film of glycerol, two fronts generally develop: a "first front" which is the first to disturb the initial film, and the "unstable front" which follows the first front and displays instabilities. We have found that power laws are indeed a suitable fit to the radial spreading data for both the first front and the unstable front. The parameters of the power law fit are affected by both concentration and humidity. An increase in concentration across constant humidity leads to higher coefficients and lower powers. An increase in humidity across constant concentration also leads to higher coefficients and lower powers, probably through the effect of increasing the water content and hence decreasing the viscosity of the glycerol film.

We have also shown that the purely visual aspect of spreading patterns of varying humidities are drastically different. The spreading of samples in higher humidities leads to more generations of bifurcations, and hence a more complicated and fractal-like pattern. The spreading of surfactants in lower humidities, on the other hand, does not exhibit multiple generations of bifurcations and looks more like a flower with petals.

Varying the volume of surfactant deposited does not change the fractal dimension of the spreading pattern. Higher volumes do, however, lead to slightly higher powers and lower coefficients in the power-law fits of radial spreading.

We report fractal dimensions between 1.45 to 1.65. The "true" fractal dimensions in which multiple generations of bifurcations happen have a fractal dimension of approximately 1.65.

6.2 Recommendations

First some suggestions to those who wish to continue this experiment. Firstly, be very aware of the humidities in which you are working. I was personally astonished at the factor at which humidity played in a role in my spreading patterns. The best way to carry out this experiment is to keep a cell in which you can control the humidity, and carry out your experiment within this cell. Additionally, make sure that the humidity of the cell is in equilibrium with the glycerol film such that your glycerol film will not absorb water throughout the course of the experiment. Glycerol is much more hygroscopic than you might have guessed. And especially on a thin film, water absorption happens very quickly.

If one wishes to pursue further theory on this topic, I recommend investigating the issue of concentration affecting the powers in the power-law fits of radial spreading. The current theory provides no explanation for how or why a change in concentration could possibly affect the power, although as I have discussed in the Analysis chapter, Jensen and Grotberg [20] provide a potential point of breakthrough on this topic. If one can provide a solid explanation and derivation on how concentration and power of spreading are related, this would prove extremely useful.

If one wishes to pursue further experiments on this topic, one possibility is to study how varying the film thickness affects the spreading power laws. Although I did not study the effect of varying film thicknesses, I suspect that film thicknesses affect the power of the spreading power laws. This is not a theory that has been made nor tested, to my knowledge. However, the fact that previous experiments have confirmed the $r \sim t^{1/4}$ power law rate for spreading on thicker films of 25 μm to 0.98 mm, yet my experiment as well as Troian's [39] find spreading power law rates of approximately $r \sim t^{0.7}$ for micron films seems to imply that a change in the thickness of the substrate affects the spreading power laws. This is something that could be of interest for a future experiment: to study how the thickness of the underlying film affects the spreading laws.

A final suggestion I will make of a potential experiment to perform on this topic is how the

viscosity of the underlying film affects the spreading patterns and instabilities exhibited by the spreading surfactants. As has been suggested by my experiments (assuming our humidity affecting viscosity claim is correct), humidity plays a large role in determining the types of instabilities exhibited by the spreading surfactants. Lower viscosities in the film seem to lead to more ramified fingering, whereas higher viscosities in the film seem to inhibit the mobility and hence bifurcations of the spreading surfactant. Not that the instabilities exhibited in this system are already well-explained or understood, but I personally think it would be interesting to see what kind of role viscosity alone plays in the instabilities. Perhaps that will even pave a path to revealing why and how the instabilities appear and develop at all.

Bibliography

[1] *Anionic surfactants, volume 7, Surfactant Science Series.*

[2] Neonatal respiratory distress syndrome. *PubMed*, May 2011.

[3] P. F. Luckham A. B. Afsar-Siddiqui and O. K. Matar. Unstable spreading of aqueous anionic surfactant solutions on liquid films. part 1. sparing soluble surfactant. *Langmuir*, 19(696-702), 2003.

[4] O. K. Matar A. D. Dussaud and S. M. Troian. Spreading characteristics of an insoluble surfactant film on a thin liquid layer: comparison between theory and experiment. *J. Fluid Mech.*, 544, 2005.

[5] F. T. Bonner A. G. Emslie and L. G. Peck. Flow of a viscous liquid on a rotating disk. *Journal of Applied Physics*, 29(5), 1958.

[6] J. Ahmad and R. S. Hansen. A simple quantitative treatment of the spreading of monolayers on thin liquid films. *J. Colloid Interface Sci.*, 38(601), 1972.

[7] A. A. Darhuber B. J. Fischer and S. M. Troian. Streamlets and branching dynamics in surfactant driven flow. *Phys. Fluids*, 13(9), 2001.

[8] C. J. Fox D. W. Fallest, A. M. Lichtenberger and K. E. Daniels. Fluorescent visualization of a spreading surfactant. *New J. Phys.*, 12, 2010.

[9] Adrian Daerr. An imageJ plug-in for surface tension measurement through the pendant drop method. *Goutte_pendante*, September 2011.

[10] A. A. Darhuber and S. M. Troian. Marangoni driven structures in thin film flows. *Physics of Fluids*, 15(9), 2003.

[11] B. Frank and S. Garoff. Origins of the complex motion of advancing surfactant solutions. *Langmuir*, 11(87), 1995.

[12] B. Frank and S. Garoff. Surfactant self assembly near contact lines: Control of advancing surfactant solutions. *Colloids Surf. A*, 116(31), 1996.

[13] R. W. Gallant. Hydrocarbon processing. 46(5):201–215, 1967.

[14] D. P. Gaver and J. B. Grotberg. The dynamics of a localized surfactant on a thin film. *J. Fluid. Mech.*, 213(127), 1990.

[15] Nach Gerlach. *Chemische Industrie*, 9, 1884.

[16] D. W. Grover and J. M. Nicol. The vapor pressure of glycerin solutions at twenty degrees. *Journal of the Society of Chemical Industry*, 59, 1940.

[17] S. He and J. B. Ketterson. Surfactant driven spreading of a liquid on a vertical surface. *Phys. Fluids*, 7(11), 1995.

[18] J. S. Huang. *Journal of Surface Science Technology*, 5(3):83–131, 1989.

[19] Salama Ibrahim. Corrosion inhibitors in the oilfield, May 2011.

[20] O. F. Jensen and J. B. Grotberg. Insoluble surfactant spreading on a thin viscous film: Shock evolution and film rupture. *J. Fluid Mech.*, 240(259), 1992.

[21] V. G. Levitch. *Physiochemical Hydrodynamics.* Prentice Hall Inc, 1962.

[22] V. Ludviksson and E. Lightfoot. Electrochemical processes in thin films. *Journal of The Electrochemical Society*, 113(12), 1966.

[23] R. V. Craster M. R. E. Warner and O. K. Matar. Fingering phenomena associated with insolublesurfactant spreading on thin liquid ms. *J. Fluid Mech.*, 510, 2004.

[24] Benoit B. Mandelbrot. *The Fractal Geometry of Nature.* W. H. Freeman and Company, 1982.

[25] C. Marangoni. *Ann. Phys. Chem. (Poggendorff)*, 143(337), 1871.

[26] A. Marmur and M. D. Lelah. The spreading of aqueous surfactant solutions on glass. *Chem. Eng. Commun.*, 13(133-143), 1981.

[27] O. K. Matar and S. M. Troian. Dynamics and stability of surfactant coated thin spreading films. In *Dynamics in Small Confining Systems III by J. M. Drake, J. Klafter and E. R. Kopelman, Eds*, volume 464. 1996.

[28] O. K. Matar and S. M. Troian. Linear stability analysis of an insoluble surfactant monolayer spreading on a thin liquid film. *Phys. Fluids*, 9(3645), 1997.

[29] O. K. Matar and S. M. Troian. Growth of non-modal transient structures during the spreading of surfactant coated films. *Phys. Fluids*, 10(1234), 1998.

[30] O. K. Matar and S. M. Troian. The development of transient fingering patterns during the spreading of surfactant coated films. *Phys. Fluids*, 11(3232), 1999.

[31] O. K. Matar and S. M. Troian. Spreading of a surfactant monolayer on a thin liquid film: Onset and evolution of digitated structures. *Chaos*, 9(141), 1999.

[32] Omar K. Matar. *Spreading Behavior of Thermally Driven Liquid Films.* PhD thesis, Princeton University, 1998.

[33] E. R. Ramer O. M. Ogunsola and D. H. Smith. Analysis of viscous fingering in two-dimensional flow cell by fractal dimension. *National Energy Technology Laboratory.*

[34] Ashanthi Melanie Pereira. An experimental investigation of a Marangoni-driven fingering instability in surfactant-water systems. Master's thesis, Princeton University, 1995.

[35] E.P. Perman and T. W. Price. Vapour-pressure of concentrated aqueous solutions. *Transactions of the Faraday Society*, 8, 1912.

[36] W. S. Rasband. ImageJ. U. S. National Institutes of Health, Bethesda, Maryland, USA, 1997-2010.

[37] E. Herbolzheimer S. M. Troian and S. A. Safran. Fingering instability in thin wetting films. *Phys. Rev. Lett.*, 62(1492), 1989.

[38] E. Herbolzheimer S. M. Troian, S. L. Wu and S. A. Safran. Fingering instability of a spreading drop. *Phase Transitions in Soft Condensed Matter*, 211, 1989.

[39] X. L. Wu S. M. Troian and S. A. Safran. Fingering instability in thin wetting films. *Phys. Rev. Lett.*, 6(1496), 1989.

[40] P. G. Saffman and G. Taylor. The penetration of a fluid into a porous medium or hele-shaw cell containing a more viscous liquid. *Proc. R. Soc. London A*, 245(312), 1958.

[41] Elana Schor. Ingredients of controversial dispersants used on gulf spill are secrets no more. *The New York Times*, June 2010.

[42] M. I. Shamos and D. Hoey. Closest point problems. *Proceedings of the 16th annual IEEE Symposium on foundations of computer science*, pages 151–162, 1975.

[43] M. L. Sheely. Glycerol viscosity tables. *Industrial and engineering chemistry*, 24(9), 1932.

[44] J. Slattery and E. L. Stuckey. *Trans. Roy Soc. Can. Sect.*, 26, 1932.

[45] The Soap and Detergent Association, Glycerine & Oleochemical Division, 475 Park Avenue South, New York, New York 10016. *Glycerin: an overview*, 1990.

[46] C. V. Sternling and L. E. Scriven. Interfacial turbulence: hydrodynamic instability and the Marangoni effect. *A.I.Ch.E. Journal*, 5(514), 1959.